TECHNISCHE UNIVERSITÄT WIEN
Vienna | Austria

Master Thesis

Methodology of Micro-PIV Investigation of Blood Flow in Channels with Micro-Structures

carried out for the purpose of obtaining the degree of Diplom-Ingenieur (DI), submitted at TU Wien, Faculty of Mechanical and Industrial Engineering, by

Tsvetan Yorov

Matr. Nr.: 01528255 (066 453)

under the supervision of

Univ.Prof. Dipl.-Ing. Dr.techn. Margit Gföhler

Institute for Engineering Design and Product Development

and

Ao.Univ.Prof. Dipl.-Ing. Dr.techn. Michael Harasek

Institute of Chemical, Environmental and Bioscience Engineering

Reviewed by

Univ. Prof. Dipl.-Ing. Dr. Margit Gföhler
Institute of Engineering Design and Product Development
Getreidemarkt 9
A-1060 Vienna, Austria

Ao.Univ.Prof. Dipl.-Ing. Dr.techn. Michael Harasek
Institute of Chemical, Environmental and Bioscience Engineering
Getreidemarkt 9
A-1060 Vienna, Austria

Abstract

As the medical devices industry advances in the developing and production of mechanisms and equipment for fighting disorders of the cardiopulmonary system, new engineering problems arise. Such devices are extracorporeal membrane oxygenators (ECMO), as well as external ventricular assist devices (VADs). Since, their work includes blood handling, it is important to assess how the blood is affected, while flowing through such devices.

Particle image velocimetry (PIV) is an approach to observe fluid flows in specific conditions and obtain important knowledge regarding the mechanical properties of the flow, e.g. velocity fields, shear strain/stress, etc. With the help of PIV it is possible to obtain some of the information regarding the blood flow through assistive medical devices. Moreover, predictions made with computational fluid dynamics (CFD) could be validated.

In this work a methodology for derivation of reliable data from micro-PIV experiment is established in series of experiments with simple rectangular channel. The best configuration of the system was chosen through tests with different settings, such as different interrogation windows, working fluids, particles and concentrations of particles. The results were compared to CFD simulations.

After the best conditions of the setup were found, a channel was produced to replicate the cross-section of ECMO-membrane. This channel was used to observe the transverse flow of transparent fluid, mixture of xanthan gum, sucrose and water, with viscosity similar to this of the blood. The velocity fields in between the acrylic rods, substituting the fibres, were observed at 4 different flow rates. The mean absolute percentage error (MAPE) between the experiments and respective CFD simulations was estimated between 12 and 17 %. The experimental results were further used to quantify the hemolysis between two fibres. Furthermore the blood damage was compared to theoretically estimated Sherwood number for 6 different velocities. Eventually, an optimal velocity in between the fibres was proposed, in the meaning of best mass transport on the cost of minimum blood damage.

As a last experiment, a channel with real fibres, attached parallel to the flow, was prepared. The velocity profile in the middle was compared to velocity profile from a CFD simulation of a channel with the same geometry, where the fibres are simulated as rigid bodies. The resulting MAPE was 4%.

Additionally, concepts for improvement of the methodology were included.

Kurzfassung

Mit dem Fortschritt der Medizinprodukteindustrie bei der Entwicklung und Herstellung von Mechanismen und Geräten zur Bekämpfung von Störungen des Herz-Lungen-Systems treten neue technische Probleme auf. Solche Geräte sind extrakorporale Membranoxygenatoren sowie externe ventrikuläre Unterstützungsgeräte . Da ihre Arbeit die Handhabung von Blut umfasst, ist es wichtig zu beurteilen, wie das Blut beeinflusst wird, während es durch solche Geräte fließt.

Particle Image Velocimetry (PIV) ist ein Ansatz zur Beobachtung von Flüssigkeitsströmungen unter bestimmten Bedingungen und zur Gewinnung wichtiger Kenntnisse über die mechanischen Eigenschaften der Strömung, z.B. Geschwindigkeitsfelder, Scherbeanspruchung, Spannung usw. Mit Hilfe von PIV ist es möglich, einige Informationen über den Blutfluss durch unterstützende medizinische Geräte zu erhalten. Darüber hinaus konnten Vorhersagen mit numerischer Strömungssimulation validiert werden.

In dieser Arbeit wird eine Methodik zur Ableitung zuverlässiger Daten aus Mikro-PIV-Experimenten in einer Reihe von Experimenten mit einfachen rechteckigen Kanälen festgelegt. Die beste Konfiguration des Systems wurde durch Tests mit unterschiedlichen Einstellungen ausgewählt, z. B. unterschiedlichen Abfragefenstern, Arbeitsflüssigkeiten, Partikeln und Partikelkonzentrationen. Die Ergebnisse wurden mit numerischen Strömungssimulationen verglichen.

Nachdem die besten Bedingungen des Aufbaus gefunden worden waren, wurde ein Kanal hergestellt, um den Querschnitt der Membran von einem Membranoxygenator zu replizieren. Dieser Kanal wurde verwendet, um den Querfluss von transparenter Flüssigkeit, einer Mischung aus Xanthangummi, Saccharose und Wasser mit einer ähnlichen Viskosität wie die des Blutes zu beobachten. Die Geschwindigkeitsfelder zwischen den Acrylstäben, die die Fasern ersetzten, wurden bei 4 verschiedenen Flussraten beobachtet. Der mittlere absolute prozentuale Fehler (MAPE) zwischen den Experimenten und den jeweiligen numerischen Strömungssimulationen wurde zwischen 12 und 17% geschätzt. Die experimentellen Ergebnisse wurden weiter verwendet, um die Hämolyse zwischen zwei Fasern zu quantifizieren. Darüber hinaus wurde der Blutschaden mit der theoretisch geschätzten Sherwood-Zahl für 6 verschiedene Geschwindigkeiten verglichen. Schließlich wurde eine optimale Geschwindigkeit zwischen den Fasern vorgeschlagen, im Sinne eines besten Massentransports zu den Kosten einer minimalen Blutschädigung.

Als letztes Experiment wurde ein Kanal mit realen Fasern hergestellt, der parallel zur Strömung angebracht war. Das Geschwindigkeitsprofil in der Mitte wurde mit dem Geschwindigkeitsprofil einer numerschen Simulation eines Kanals mit derselben Geometrie verglichen, bei der die Fasern als starre Körper simuliert werden. Die resultierende MAPE betrug 4%.

Zusätzlich wurden Konzepte zur Verbesserung der Methodik aufgenommen.

Affidavit

I confirm, that the issue of this thesis needs the conformation of the examination committee. I declare in lieu of oath, that I wrote this thesis and performed the associated research myself, using only literature cited in this volume. I confirm that this work is original and has not been submitted elsewhere for any examination, nor is it currently under consideration for a thesis elsewhere.

Vienna, April 1, 2020

Table of contents

I. Introduction

1. Introduction to the field and agenda

30 000 is roughly the number of patients awaiting a heart transplantation at risk of dying from severe heart failure annually and only by around 12% of all cases, transplantations are performed due to the restricted availability of heart donors [1]. Another disorder of the cardiopulmonary system related to a high mortality rate is the respiratory failure. Some of its severe forms lead to a lethal end by more than 60% of the patients [2]. A common form of treating the aforementioned conditions are mechanical assist devices such as extracorporeal membrane oxygenators (ECMO), external ventricular assist devices (VADs) or internal left ventricular assist devices (LVADs). Essential part of any of these mechanisms is the presence of an impeller, which pumps the blood through the system. Moreover, the future of these devices depends on their blood compatibility or with other words it is important to assess the level of blood trauma in order to improve the further design of blood pumps [3]. The damage on the blood, also referred as hemolysis, is induced by high stresses causing rupture in the red blood cells (RBCs) membranes, which leads to irreversible release of the haemoglobin protein – the oxygen carrier [3], [4]. First direct relation between hemolysis, magnitude of shear stress and the time of exposure to this shear stress was proposed by Giersiepen et. al. [5]. The need of estimation of shear stress inside blood pumps brings our focus to different methods of evaluating flow velocity fields.

Particle image velocimetry (PIV) is an experimental approach for direct measurement of flow velocity. With the help of it, it is possible to derive exact, quantitative information regarding fluid velocity vectors at a very large number of points simultaneously [6]. In its principle, PIV is an optical measurement system, where a sensor (usually a high-speed camera) is placed outside of the flow to capture images of the whole flow field of interest. The fluid have to be seeded with tracer particles, which are illuminated in a plane or a volume of the flow in two or more frames within short and known time interval. The resulting images are further evaluated with statistical methods such as cross-correlation functions. The advantage of PIV over the indirect measurement techniques is that it gives more detailed and reliable information about the structure of whole flow field, especially in unsteady flows [7].

Computational fluid dynamics (CFD) is a widely accepted method for virtual assessment of pressure and velocity in flow systems. It is a simple and cost-effective approach, which implies different mathematical models and methods [3] in order to bring appropriate solutions for the flow parameters depending on the needs of the specific case.

1.1. Research question

The goal of this master thesis is to establish a reliable methodology for testing of flow fields in micro-channels with the help of micro-PIV. In order to succeed with this task, one has to carefully review and adjust the respective settings distinctive to a micro-PIV system.

Moreover, the experiment methodology should be developed to investigate properties of blood flow in a membrane module. For this purpose, a suitable geometry mimicking the inside of such module should be built. Since it is established, with the help of CFD (see fig. 1.1), that the transverse flow through the fibres in the membrane has the highest contribution to the mass transport in ECMO, the orientation of the fibres (normal to the plane of view) should be considered. Another obstacle in front of such an experiment is the need of a transparent blood analogue in the meaning of a fluid with mechanical properties of blood (e.g. viscosity), but pervious to the light signal in the micro-PIV. Once this requirements are met, the aforementioned CFD results represented on figure 1.1 can be validated. Furthermore, important biomedical properties like blood compatibility and efficiency of devices related to blood handling (such as LVADs and ECMO) can be evaluated. It is well known that, both blood

damage and mass transport increase with increasing velocities in flow fields. Since this relationship is not linear, an optimal velocity between the fibres of a membrane module can be proposed.

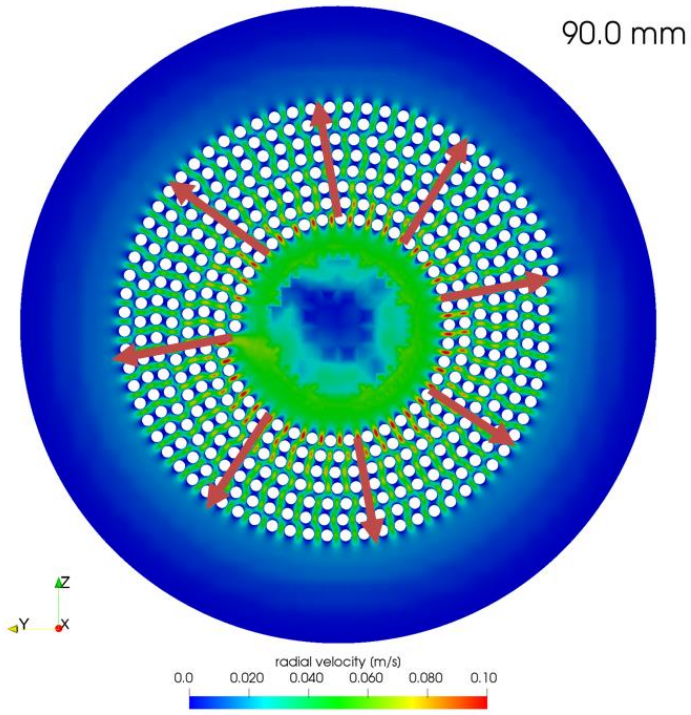

Figure 1.1 CFD simulation of the transverse flow inside an ECMO. The average velocity between the fibres is approximately 3 mm/s. Simulation is made by Benjamin Lukitsch - Institute of Chemical, Environmental and Bioscience Engineering, TU Wien, Vienna, Austria

1.2. Approach

To accomplish the set goals, first a simple channel will be built. Once the simple geometry is known, a reliable CFD simulation can be produced. Having reliable reference results to compare, different elements of the micro-PIV settings will be changed and compared how close results match with the CFD. Moreover, their influence on the measurements should be evaluated. Such settings will be the spatial resolution (interrogation window), working fluid, seeding type, seeding concentrations and the focus plane.

In order to develop the methodology for the investigation of blood flow in membrane modules, first the more complex geometry should be built. This includes different approaches for the production of such micro-structure (milling, 3D printing, etc.), together with evaluation of the influence of substitution of the real fibres with rigid materials. After choosing the best production technology and the best micro-PIV settings, the experiment can take place. The results will be again compared with CFD.

Since PIV, as concept, measures velocities, the hemolysis index will be estimated from the experimental data. However, no reliable data regarding mass transport can be extracted from this type of experiments, therefore the CO_2 transport in similar conditions will be analytically evaluated.

1.3. Structure of the thesis

In chapter II of this thesis, an overview of physiological and mechanical properties of blood is given. Next, the devices of interest related to blood handling are described, together with the important properties of mass transport and hemolysis.

The chapter continuous with a detailed review of the micro-PIV technology. Firstly, the aspects of the system are discussed, next the hardware and its specifications are commented and finally, the calculation methodology is described.

As a last part of this chapter, a brief summary of the applied numerical method is given.

In chapter III the materials and the devices used for the investigation, object of this thesis, are listed. Furthermore, the exact methodology of the experiments is described.

The results obtained from all the experiments and the simulations together with the estimations of hemolysis and mass transport are presented in chapter IV.

In chapter V the results and their success in regards to the set objectives is discussed.

Chapter VI represents a general conclusion about the work and the accomplished results.

II. Theoretical Background

2. Blood flow defining factors

This chapter summarizes the most relevant blood properties to the conducted research.

2.1. Blood composition

Blood is nonhomogeneous body fluid, which is a mixture of plasma, RBCs, white blood cells, platelets (see Figure 2.1 a) and b)), ions and proteins. Around 45% of the whole blood consists of RBCs. The other two types of cells comprise much smaller part of the blood volume with respectively 1-2 white blood cells and 50-100 platelets per 1000 RBCs or around 1% of the whole blood volume [8].

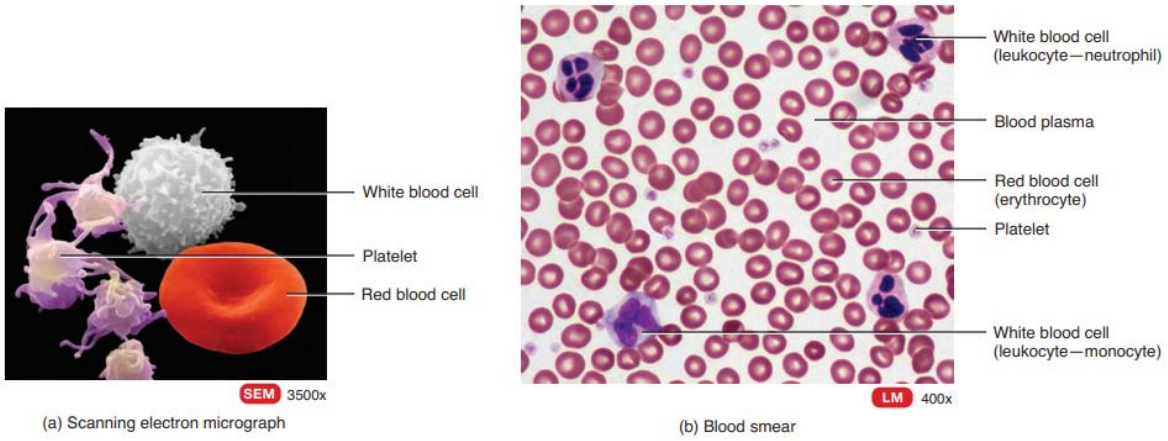

Figure 2.1 Micrographs of the main blood constituents from a) scanning electron microscope and b) light microscope. From [9]

Red blood cells (RBCs)

The RBCs, also known as erythrocytes, compose almost half of the blood volume, therefore they are the only cells that significantly influence the mechanical properties of the blood. They contain all the haemoglobin in the blood, which is about 15g per 100ml. Haemoglobin, itself, is a molecule consisting of the globin protein and an organic molecule, incorporating iron, called haem. The ability of the haem to combine reversibly with oxygen is the reason behind the large capacity of blood as an oxygen carrier (see Figure 2.2 a)).

RBCs formation takes place in the bone marrow and prior to maturation they possess nuclei. However, the nucleus is discarded upon maturation and before introduction to the circulation. The average life

span of an erythrocyte is about 120 days, however, they become more fragile with the time and end up destroyed mostly due to mechanical fragmentation caused by high shear stresses, which occur mainly in microcirculation. A RBC suspended in plasma has the shape of biconcave disc and is highly flexible. Usual dimensions are shown on Figure 2.2 b).

The structure of an erythrocyte includes a liquid interior, which is 32% solution of haemoglobin by weight with viscosity of 6mN s m^{-2}. The liquid interior is surrounded by a phospholipid membrane with thickness of around 7.5 nm. The overall density of a cell is 1080 kg m^{-3}. The liquid interior of the RBC suggest, that the shape of the cell is determined by its membrane.

If the osmotic pressure of the fluid, where the RBCs are suspended, decreases, they become spherical and lose their nutrients including the haemoglobin because of membrane rupture. However, if the ruptured cells are immersed in an appropriate isotonic solution the membrane would seal and they start to absorb and regain their original size and shape. Such RBCs are known as ghost cells due to the lack of haemoglobin and the loss of red colour. Another consequence of the liquid interior and the highly flexible membrane with behaviour close to a liquid is the ability of the erythrocyte to deform and travel along blood vessels with diameter smaller than its own [8], [10].

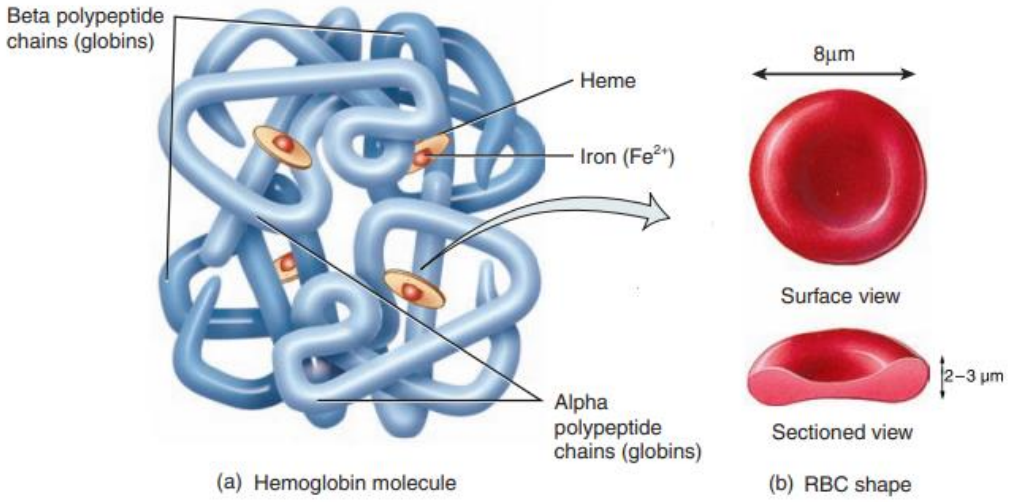

Figure 2.2 Image of a) Haemoglobin molecule and b) red blood cell. Adapted from [9]

White blood cells (WBCs)

Leucocytes, as it is commonly referred to the WBCs, are considered to almost not affect the mechanical properties of the blood since their part in the blood volume is less than 1%. They act as scavengers of microorganisms and form antibodies, which make them responsible for the defence against infections. Leucocytes usually have spherical shape with rough surface and varying diameters in the range of 7-22 µm.

The mechanical properties of WBCs are object of discussion and uncertainties. They are considered as stiffer than RBCs. Moreover, a visco-elastic behaviour of these cells is declared after observation of leucocyte flowing from a wider tube to capillary with diameter smaller than the one of the cell itself. A WBC needs between 10 and 20 s before occurring of deformation sufficient for the cell to flow along the capillary [8].

Platelets

Platelets are rounded cells without nucleus, formed in the bone marrow. They are usually smaller than RBCs and WBCs with diameter of 2-4 μm and volume of 5-10 μm^3. With their number greater than the leucocytes but still much less than the erythrocytes, they have negligible effect on the mechanical properties of the blood. Platelets are known for their ability to aggregate in the presence of adenosine diphosphate (ADP) and form clots usually in order to prevent bleeding from damaged or cut vessels [8].

Plasma

Plasma is an amber fluid consisting of 90% water by volume, 7% protein, and other inorganic and organic substances such as electrolytes, hormones and nutrients. Plasma with removed clotting factors is called serum. Moreover, the proteins suspended into the plasma are with high molecular weight, which prevents them from passing capillary wall. Thus, they stay in the blood vessel and create osmotic pressure. The biggest contributor to this pressure is protein called Albumin. Osmotic pressure might cause cell swelling and membrane rupture to the RBCs due to a water diffused into the cell interior [10], [11].

2.2. Haemodynamics and blood circulation

Blood has four main transport functions: transport of oxygen and CO_2, waste, nutrients and heat. The path of the blood goes consecutively from the heart through arteries, arterioles, capillaries, venules, veins and back to the heart. The different dimensions of the blood vessels naturally affect the physical properties of the blood flow in them.

As it can be seen at Figure 2.3 the blood leaves the heart after a contraction of the left ventricle. Due to the rapid heart systole blood is ejected with both high pressure and velocity which decrease later because of the increase of the total cross-sectional area in the capillaries. However, there is another measure that gives more information regarding the forces governing the fluid motion in the individual vessels, namely the Reynolds number (Re).

$$Re = \frac{uL}{\nu} \tag{1}$$

Where u is the velocity of the fluid L is the characteristic linear dimension and ν is the kinematic viscosity of the fluid. High Re means flow dominated by inertial forces and respectively low stands for flow governed by viscous forces. Since the Reynolds number is proportional to the characteristic length of the vessel and reciprocal to the viscosity of the fluid, it is obvious that in large blood vessels like arteries and veins, the flow is inertial but it becomes viscous when it comes to capillaries and venules. Moreover, the blood flow in large vessels is considered to be Newtonian, whereas in vessels with diameter close to the dimensions of a RBC the flow becomes non-Newtonian [8], [10], [14]. A consequence that serve as a proof of the non-Newtonian origin of the blood flow is the Faharaeus-Lindqvist effect. This effect is expressed in the formation of a plasma layer in vessels with diameter smaller than 300 μm (left-hand side of Figure 2.3) [15]

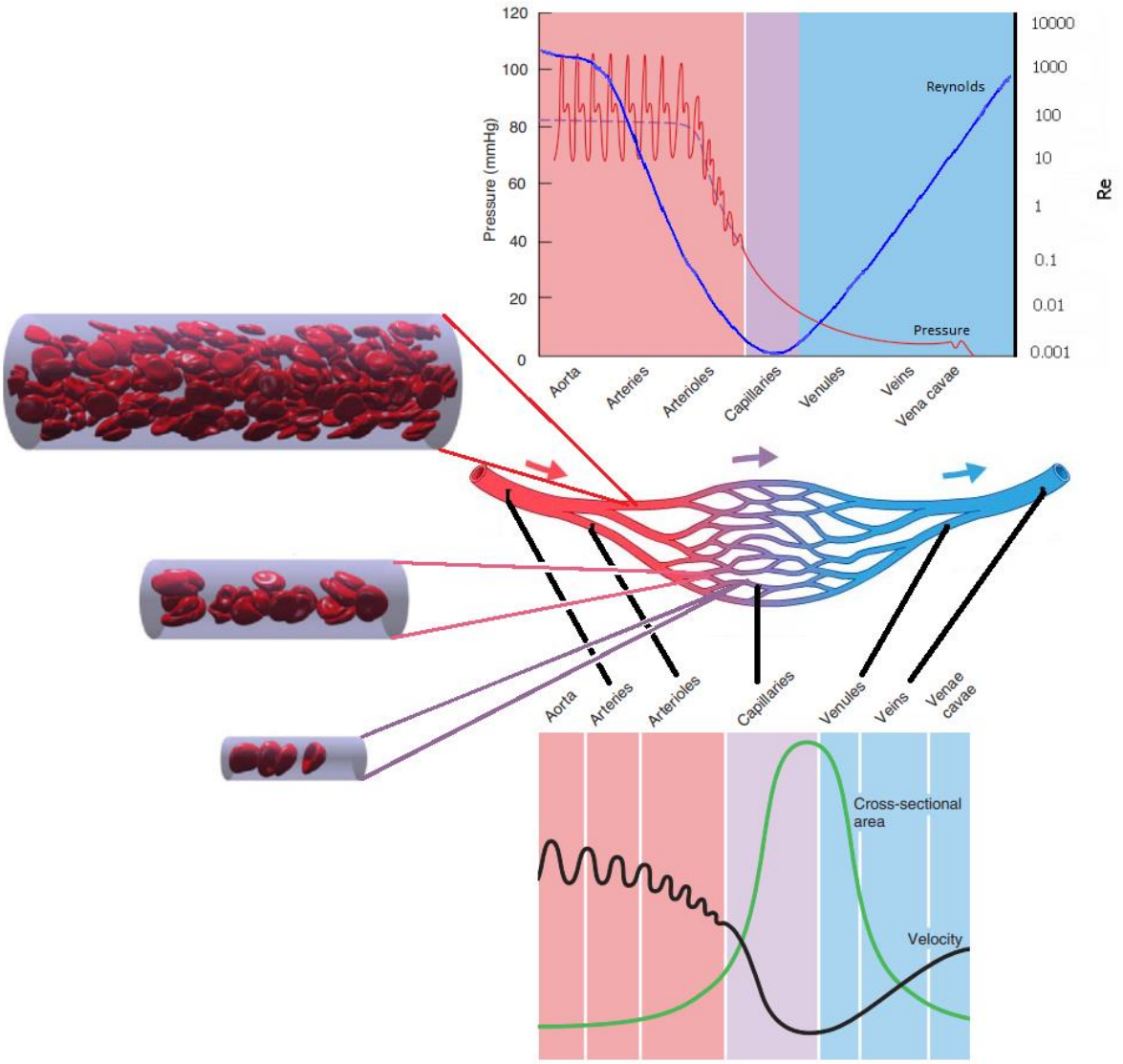

Figure 2.3 Change of the pressure, velocity, Reynolds number, and the total cross-sectional area along the different blood vessels (right) and the distribution of the RBCs stream with the decrease of size of these vessels (left). Adapted from [9], [12], [13]

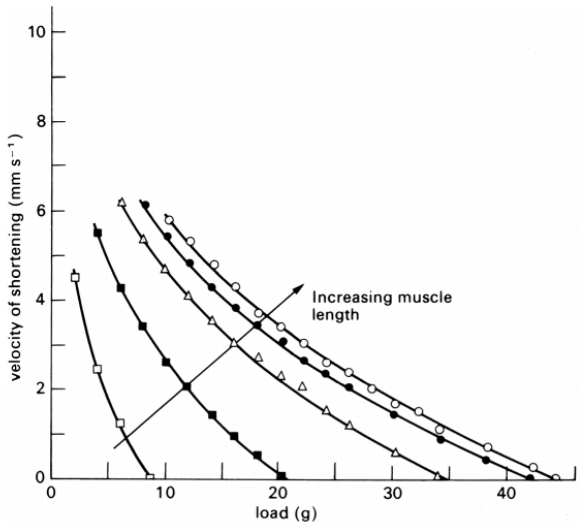

Figure 2.4 Curve of depicting the length dependence of the force velocity relationship in cardiac muscle. From [8]

2.2.1.Left ventricular assist devices (LVADs)

The normal work of the heart, characterized by some of the previously reviewed properties like pressure together with other important aspects like stroke volume, hearth pace, etc. can be altered due to pathological events. Conditions like myocardial infarction or pure mechanical overloading often lead to dysfunction of cardiac muscle and consequently to enlargement of the ventricular cavity in response to decreased ejection fraction. However, the aftereffect of the ventricular dilation is related to an increased load on the cardiac muscle (see Figure 2.4) and a high mortality rate. Moreover, remodelling of the heart by the means of molecular, cellular, biochemical, and structural changes of the myocardium is often observed in patients with heart failure. There is evidence from clinical studies that LVADs improve the health of patients and even reverse the pathological remodelling by unloading of the left ventricular [16]–[19].

LVAD is, for instance, a surgically implanted pump, which draws blood from the left ventricular apex and delivers it to the ascending aorta. There are devices using centrifugal pumps, delivering a pulsatile flow and such using turbine pumps resulting in a continuous flow (see at Figure 2.5). Both types are usually driven by an external system controller and a power source [20].

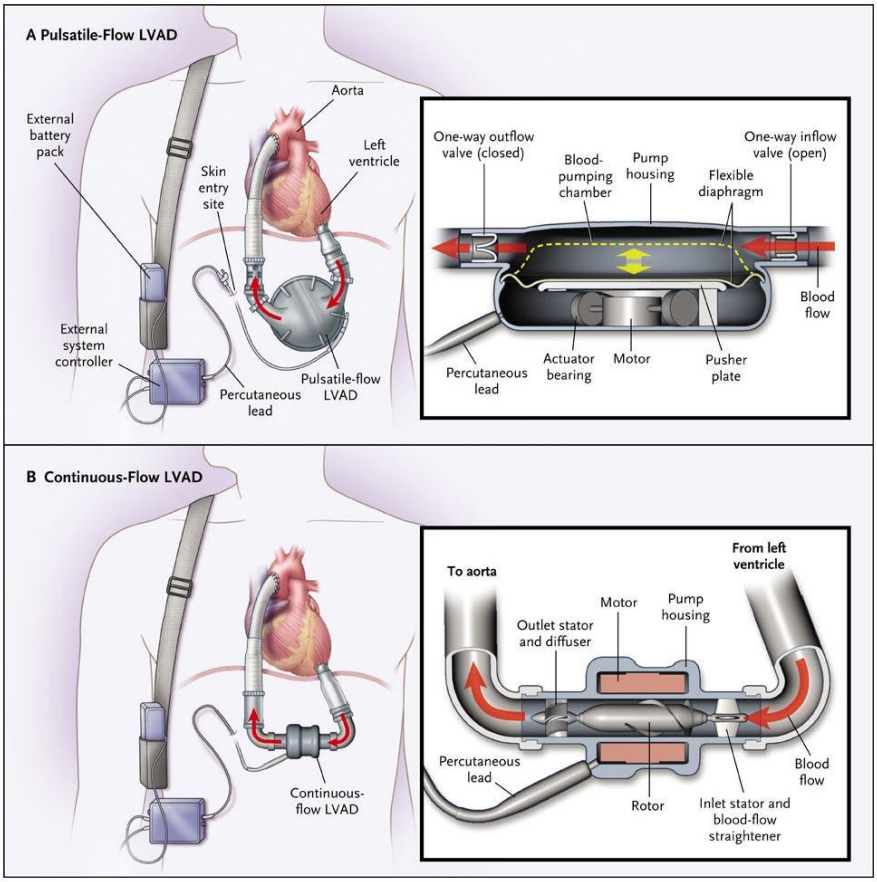

Figure 2.5 Principle setup of A pulsatile-flow LVAD and B continuous-flow LVAD. From [20]

2.3. Blood rheology

Viscosity is a measure of the internal friction within a moving fluid and is defined as the ratio of shear stress and shear rate. Shear stress is the sliding force per unit area of contact between two layers of the flow with infinitesimal thickness (also known as laminae). Shear rate is the change of velocity per unit distance radially, considering flow in a tube [14] or the rate at which laminae move past each other in

more general sense. Fluids, like water or blood plasma, where the relationship between shear stress and shear rate is linear, are referred to as Newtonian fluids.

As stated earlier, blood behaves like a Newtonian fluid in large vessels. However, this behaviour is strongly influenced by change of some conditions and properties. Important factor for the apparent viscosity of the whole blood is the presence of RBCs. The volume part of the RBCs to the whole blood volume is called haematocrit (see Figure 2.6 A).

Moreover, there are two more factors that contribute for the non-Newtonian behaviour of the blood. These are the change in the tube diameter, considering flow in tube (see Figure 2.6 C) or in the dimensions of the cross-section, considering general case and the change of the shear rate (see Figure 2.6 B). The graph on figure 2.6 B is interpreted by the fact that at low shear rates blood forms rouleaux and even aggregates in a tangled network of RBCs at shear rates near to zero. Responsible for this aggregation are the fibrinogen and globulin proteins suspended into plasma. With the increase of the shear rate RBCs spread back into a free formation and respectively the viscosity decreases [8], [14].

The relationship on Figure 2.6 C is a consequence of the Faharaeus-Lindqvist effect. In their work, Faharaeus and Lindqvist observe that the haematocrit and the viscosity in microtubes with diameters less than 300 μm are lower than these of the feed fluid [15]. Reason for this is the single-file flow pattern observed in the capillaries and the formation of a peripheral plasma layer in the arterioles. Moreover, the formation of the plasma layer near the wall is explained with the axial migration of the RBCs to the centre of the blood vessels. This has a great effect on the viscosity reduction, since shear rates are highest exactly at the periphery. The Faharaeus-Lindqvist effect on the viscosity reduction is observed down to diameters of approximately 6 μm which is comparable to the dimensions of a single RBC. Also with an increase of the scale of the tube the thickness of the marginal layer becomes insignificant relative to the tube radius, thus the effect disappears [14].

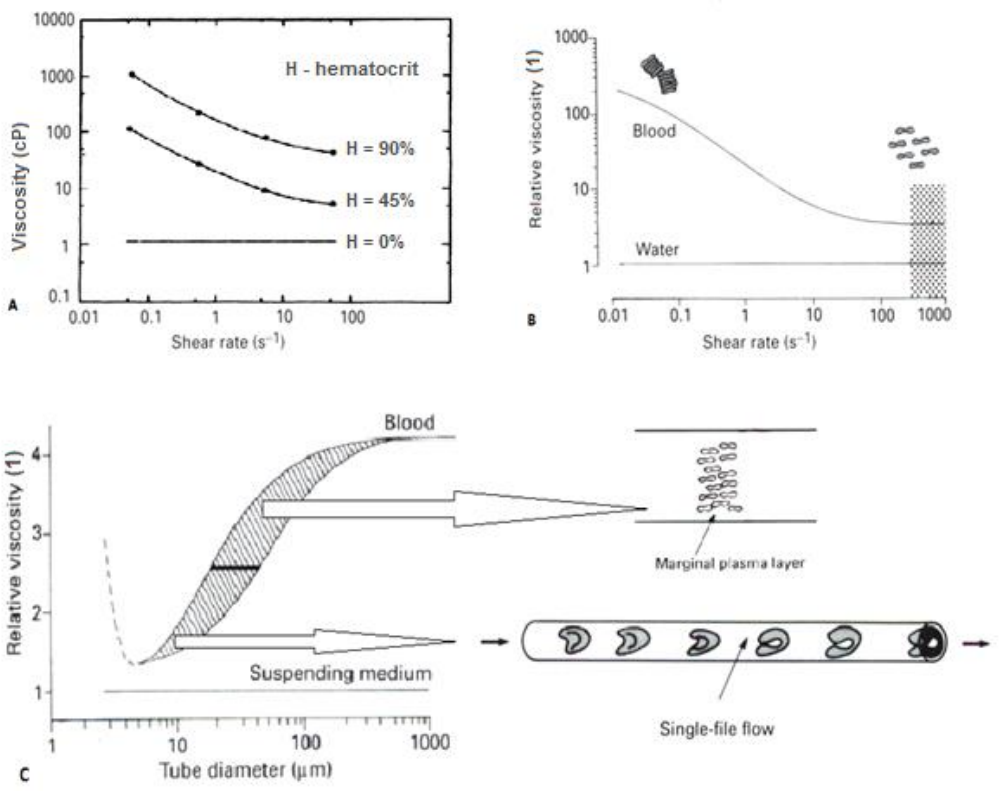

Figure 2.6 Dependence of the viscosity on A haematocrit, B shear rate, C tube radius. Adapted from [10], [12]

2.4. Velocity profiles

A steady flow in long capillary tubes is usually characterized by the Poiseuille law. The velocity profile of such a flow is parabolic in shape, with velocity at its maximum in the middle of the tube and progressively decreasing to zero at the wall (see Figure 2.7a). This is also called an axisymmetric flow [8]. However, in the case of a non-Newtonian fluid like blood it is not always like that. Along the years there have been many experimental assessments of blood velocity profiles. Some of them suggest a parabolic profile indeed [21]. Others like Goldsmith et al. reported blunt profiles (see Figure 2.7b) and even made a correlation between properties like haematocrit, flow rate and tube radius and the degree of "bluntness" of the profile [22], [23]. Lima et al. made an experiment with a microchannel with a rectangular profile and declared parabolic profiles on his side [24]. The discrepancy of the results of the different research groups underlines the complex nature of the problem. Moreover, the previous experience gives indications on the high importance of parameters like microchannel geometry, shear rate, flow rate, suspension fluid, concentration of seeding particles, experimental errors [25].

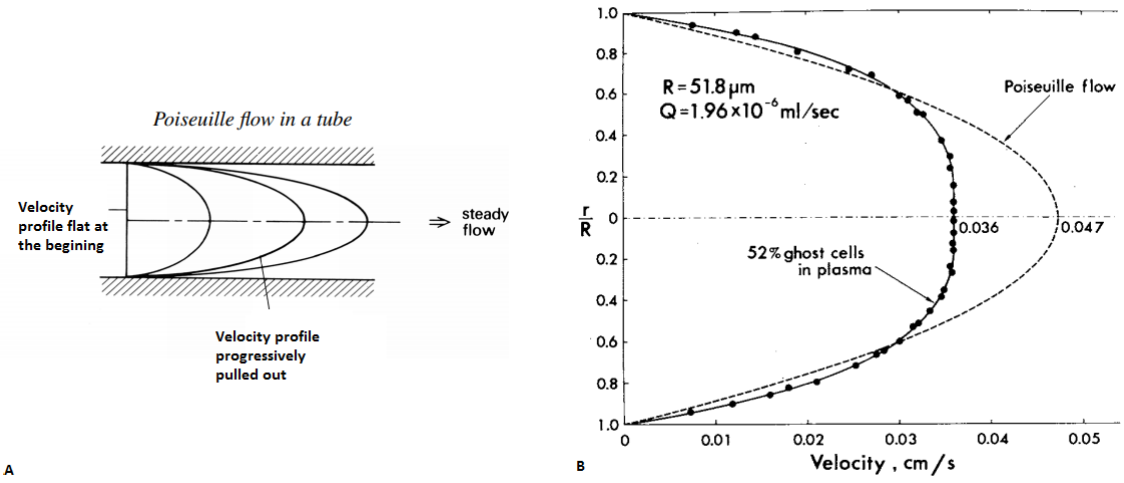

Figure 2.7 A Schematic representation of Poiseuille flow development. Adapted from [8]. B Blunt velocity profile of ghost cells suspended in plasma, where R is the radius of the tube, r is the distance to the point of measurement and Q is the flow rate. From [23]

2.5. Blood oxygenation

Main purpose of the blood circulation is to ensure the movement of substances between the blood and the interstitial fluid – the capillary exchange. The mechanism standing behind the exchange of oxygen (O_2) and carbon dioxide (CO_2) is simple diffusion. Nutrients and O_2 are usually in a higher concentration in the blood so they diffuse down their concentration gradient into the interstitial fluid and then into the body cells, whereas CO_2 and waste products released by the body cells are in higher concentration in the interstitial fluid, thus they diffuse into the blood [9]. Moreover, the exchange of substances between mediums due to diffusion is called mass transfer or mass transport.

2.5.1.Mass transport

Mass transport is determined by Fick's law that states that whenever there is a concentration gradient of a given material within a medium, there is a flux of the material towards the regions of a lower material concentration. This flux is proportional to the concentration gradient and the coefficient of this proportionality is called diffusion coefficient of the material. However in some practical situations is impossible to consider transport rates simply in terms of a molecular diffusivity. In such cases we consider an overall mass transport coefficient that includes all diffusion pathways, e.g. through cell membranes. [8]. The oldest and simplest approach for mass transport evaluation is the film model (see Figure 2.8). In this model the entire concentration gradient between the bulk of the fluid and the surface is localized in a viscous thin layer. This model suggest that the mass transport coefficient k_c equals the diffusion coefficient D_{AB} divided by the film thickness δ. Obvious drawback of this model is the practical inability to determine the layer thickness considering parabolic profiles.

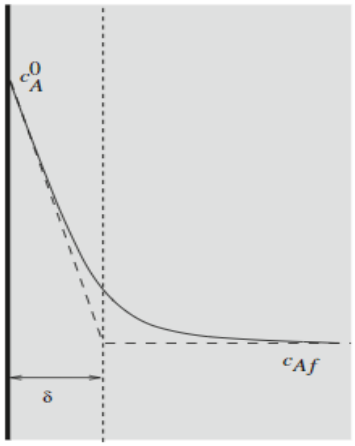

Figure 2.8 Concentration profile near an interface, where δ the film thickness, and c_A^0 and c_{Af} are the concentrations of the compound A respectively at the surface and the bulk of the fluid. From [26]

There are some more reliable approaches for determination of the mass transport existing, based on dimension analysis, boundary layer theory and penetration theory, however the details regarding them are not in the scope of this work.

In practice mass transport coefficients are often characterized by the use of dimensionless numbers such as Sherwood number, Reynolds number and Schmidt number, weighted by experimentally derived coefficients.

The Sherwood number (Sh) is defined as:

$$Sh = \frac{k_c L}{D_{AB}} \tag{2}$$

where k_c is the mass transport coefficient, L is the characteristic length and D_{AB} is the effective diffusion coefficient of the substance of interest in the respective medium. The physical meaning of the Sherwood number can therefore be described as the ratio of convective to diffusive mass transport.

The Reynolds number (Re), given as in (1), chapter 2.2, characterizes the fluid motion conditions and the Schmidt number (Sc) is the ratio between the momentum diffusivity and the mass diffusivity, given as:

$$Sc = \frac{\nu}{D_{AB}} \tag{3}$$

where ν is the kinematic viscosity of the fluid and D_{AB} is again the same diffusion coefficient as in (2).

From the aforementioned combination of boundary layer theory, penetration theory, etc., the mass transport can be theoretically characterized with the Sherwood number as [26]:

$$Sh = f(Re, Sc) \tag{4}$$

2.5.2.Extracorporeal membrane oxygenators (ECMO)

ECMO is a part of the continuously evolving mechanical circulatory support. They can be used in veno-arterial configuration usually for treatment of cardiac failure and in veno-venous mode respectively for respiratory failure [27]. The main design purpose of an ECMO circuit (See figure 2.9) is to pump and

oxygenate blood and remove CO_2. First important part of the design is the pump (See figure 2.9 C). The main part of interest is the gas exchange membrane. There are two different types of oxygenators – silicone membrane oxygenator and hollow fibre oxygenator (HFO) represented respectively on figure 2.9 A and B. In the silicone membrane oxygenator a thin silicone sheath is separated by a plastic screen spacer. The silicone sheaths are wrapped around a polycarbonate core and housed in a silicone sleeve. Blood flows on the one side of the membrane while sweep gas is flowing in the opposite direction on the other side of the membrane. HFO consist of capillary tubes and exchange gas via counter current mechanism similarly to the silicon membrane mechanism. HFO has the advantage of reduced clot formation because of its coating, reduced platelet activation and inflammation because of a lesser surface area, and a decreased shear stress on RBCs because of the lower pressure gradient across the membrane. Other parts of ECMO are heat exchanger, bridge between the venous and arterial components, injection of heparin (or albumin) to suppress of inflammatory reactions [28].

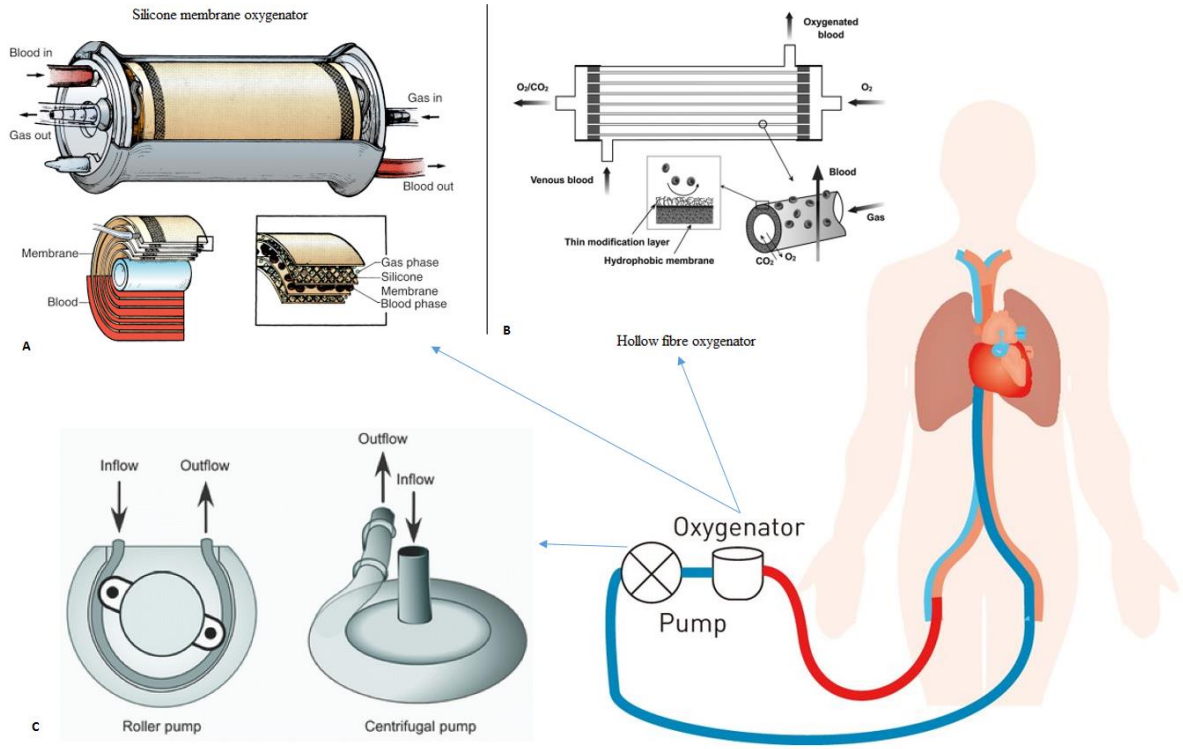

Figure 2.9 Schematic representation of veno-venous ECMO circuit with different types of membrane oxygenators and pumps – A silicone membrane oxygenator, B hollow fibre oxygenator and C roller and centrifugal pump. Adapted from [29]–[32].

2.6. Hemolysis prediction

As it was mentioned earlier, flow-induced hemolysis is a crucial issue for the development of blood-transporting devices. There have been many quantitative models proposed for the estimation of hemolysis in the last decades. However, their accuracy and reliability is questionable. The existing models differ in two central aspects – firstly, they are either stress-based or strain-based and next, they are established using Langrangian methods, where analysis is done following the flow, or Eulerian method, where observation is fixed within the flow space. Stress-based models rely on empirical relations between the local instantaneous hemolysis and the local instantaneous stress, whereas strain-based models are more advanced and include more variables and parameters, e.g. extension of RBC membrane, RBC deformation, etc [4].

Important part for the stress-based models is to define equivalent stress for the hemolysis. The problem arises from the requirement that a single parameter will be responsible for multi-dimensional shear

conditions described by a stress tensor. Popular approach in the literature is the use of the second invariant of the viscous stress tensor τ [4]:

$$II_\tau = \frac{1}{2}\left[\left(tr(\tau)\right)^2 - tr(\tau^2)\right] \tag{5}$$

Furthermore, a whole criterion group is created using the square root of the second invariant multiplied by a negative factor:

Table 2.1 Different sets of parameters relating hemolysis to shear stress and exposure time.

	C	α	β
GW	3.63×10^{-7}	2.416	0.785
HO	1.8×10^{-8}	1.991	0.765
ZT	1.228×10^{-7}	1.9918	0.6606

$$\overline{\tau}_i = \sqrt{-n\, II_\tau} \tag{6}$$

Criterions using $n = 3$ (which equals the so called von Mises criterion) and $n = 2$ were introduced by Bludszuweit et al. [33], [34]. However, in cases of one-dimensional shear flow the von Mises relation would return the shear stress times $\sqrt{3}$ [4]. In order to obtain an uniform shear stress in such cases a factor of $n = 1$ is introduced [35]. More definitions of an equivalent shear stress can be found in the literature and the choice of an appropriate one have an important role on the final result obtained from the hemolysis prediction model [4].

An extensive review on the hemolysis prediction was done by Yu et al. [4] including 7 different models from the literature and one derived formulation. The analysis incorporates both strain- and stress-based models in Langrangian and Eulerian formulation. Here, only the original model introduced, firstly, by Giersiepen et al., will be reviewed because of its simplicity, easy implementation and relatively high correlation to the experimental results. As it was mentioned earlier this model is a direct relation between hemolysis, magnitude of shear stress $\overline{\tau}$ and exposure time t:

$$H(\overline{\tau}, t) = C\, \overline{\tau}^{\alpha} t^{\beta} \tag{7}$$

Here H stands for the ratio between the released haemoglobin and the total haemoglobin ($\Delta Hb/Hb$). C, α and β are parameters obtained from fitting experimental data. The first set of parameters was obtained from the research of Wurzinger et al. [36]. His group submitted human RBCs to a shear stress with values up to 255 Pa held constant in time and exposure time of up to 700 ms. The obtained results (see Table 2.1 - GW) used in eq. 7 were declared to overestimate hemolysis at least in order of magnitude [37]–[39]. In general this parameter set is still widely in use because of the drawbacks of the alternative, e.g. the use of animal RBCs for the experiments. Moreover, it is a good approximation by similar values of the shear stress and the exposure time as in the original experiment [4].

Alternative parameter set (See Table 2.1 - HO) has been proposed employing the experiments of Heuser and Opitz [40]. In their work porcine blood was tested with a shear stress between 30 and 600 Pa and exposure time between 3.4 and 690 ms. One more set (see Table 2.1- ZT) was obtained by Zhang et al. [41]. Here the subject of the experiment was ovine blood examined under a shear stress between 30 and 320 Pa and exposure times between 0.03 and 1.5 s. An important issue of the latter two sets is the use of animal blood in the experiments in which they were obtained. The problem comes from the different properties of the animal RBCs compared to these of a human.

3. Particle Image Velocimetry (PIV)

Particle image velocimetry is an important method of the modern experimental fluid dynamics. It is a technique for velocity field measurement in fluid systems. Specifically, in the case of a double-pulsed PIV, tracer particles are illuminated by either a pulsed light source or a continuous light source with combination of a mechanical or electronic shutter that covers the camera, which captures the position of the particles at two known moments in time. The two consecutive images are correlated and the displacement of the particles is evaluated from them. With increasing the spatial resolution of such measurements in custom-prepared geometries, PIV becomes a very useful tool in both engineering and purely scientific fields. Respectively, it becomes the key to evaluate flow properties in microfluidic

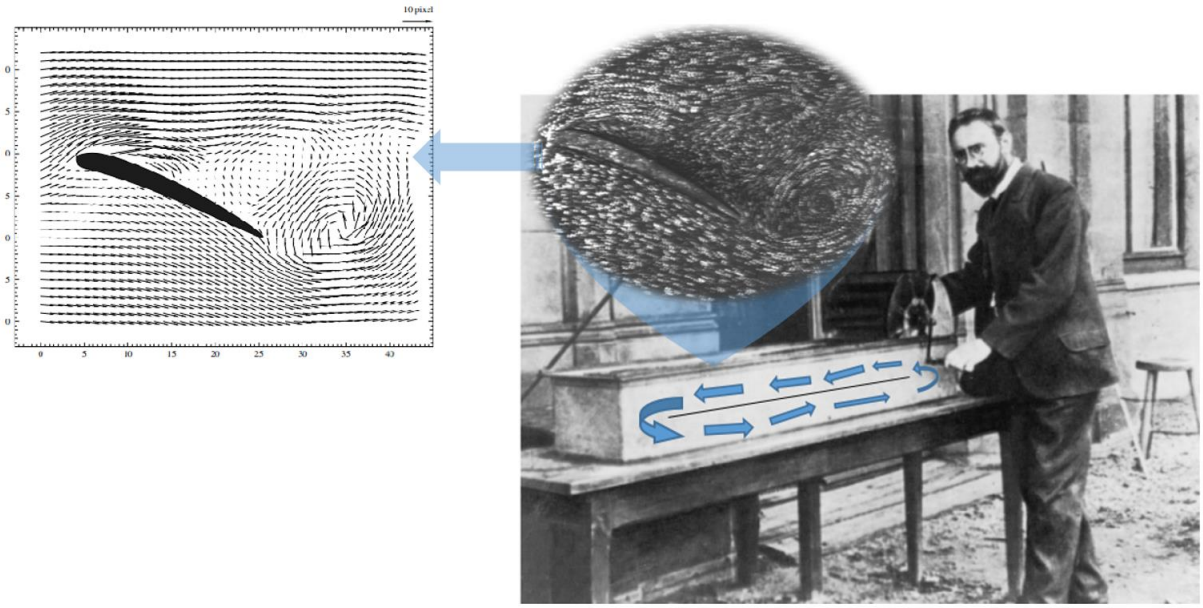

Figure 3.1 Ludwig Prandtl next to his water tunnel (1904). The picture of the flow is a replica of a flow behind a wing in Prandtl's tunnel made with modern equipment. Furthermore, a corresponding vector map of the instantaneous velocity field is derived. Adapted from [7].

devices, as well as to enhance the scientific methodology for revealing detailed information regarding microscale transport processes [42].

Different PIV techniques have been used for assessment of blood properties *in vitro* in microchannels [25], *in vivo* in an arteriole of a rat [43] as well as for estimation of flow and validation of CFD flow simulations in blood pumps [44]–[47]. They managed to take quantitative measurements of important physical properties, such as velocity, stress, strain rate, vorticity. Moreover, phenomena related to biological nature of the blood flow are observed, e.g. single RBC motion, behaviour of RBCs with regards to the changing geometry of the flow channels. From an engineering point of view, the influence of different kind of pumps (axial, rotary, etc.) on the blood properties and the hemolysis are evaluated. Different methodologies like conventional micro-PIV, confocal micro-PIV, micro-PTV with different setup properties (suspension fluid, tracer particles, channel materials and geometries, haematocrit etc.) are compared. However, there is not much information about blood flow in membrane modules and suitable methodology for building an appropriate experimental loop for such investigations.

The following chapter gives an overview on the most important aspects of a PIV configuration relevant to investigations of biofluids in microscale.

3.1. Historical development

First steps towards experiments for visual flow tracking were made by Ludwig Prandtl in the beginning of the 20th century. He designed a water tunnel divided into upper and lower section by a horizontal wall

and a manually driven blade wheel, which circulates the water from the bottom section to the top one forming a closed loop. Since the upper section was open, one could mount obstacles such as cylinders, prisms or wings in it. The flow structure was visualized and further studied by suspending mica particles on the water surface [48], [49]. Although Prandtl managed to manipulate some of the parameters in his experiments like the type and position of obstacle, flow velocity or steady-unsteady flow, he could only make qualitative conclusions regarding the flow field. At this time, it was still impossible to gain a quantitative data about flow velocity through observation. However, the technical progress from the last 20 years in the fields of optics, lasers, electronics including digital capturing and computer technology made it possible to extract quantitative information on complex velocity fields even from setups similar to the one from Prandtl (see figure 3.1). [7].

3.2. General aspects

Here the most important aspects of the PIV technique will be outlined before getting into more detailed analysis of the technical solutions in the next chapter.

PIV is an optical observation technique conducting *non-intrusive velocity measurements*, which means that it does not disturb the flow in contrast with the case of use of probes like pressure tubes or hot wires [7].

PIV does not directly measure the velocity of the flow, but the velocity of particles, usually introduced preliminary to the flow, or with other words PIV is an *indirect velocity measurement* [7].

Since it is able to capture images of large areas of the flow and extract velocity fields out of them, PIV is considered as a *whole field technique*. This feature makes it unique because the most of the other techniques measure velocity only in a single point [7].

The fact that the velocity of the tracing particles is measured and not the flow itself is a reason to consider a *velocity lag*. This lag is consequence of the inability of the particles to follow the flow accurately.

Another important aspect is the *illumination* of the particles. Smaller particles follow the flow more precisely but on the other hand, their light scattering efficiency is low. Big particles have better light scattering properties but they are not reliable flow tracers. A compromise between the size of the particles and the power of the light source has to be found. As part of the illumination an appropriate dur*ation of the light pulse* should be chosen in order to avoid blurred images. Moreover, the *time delay between the pulses* should be adjusted to be short enough so the particles moving also in out-of-plane direction do not leave the illuminated plane, but enough time for a sufficient displacement should be considered as well. [7].

Considering tracer particles for a PIV application, a homogenous *distribution of particles in the flow* is desirable in order to obtain optimal evaluation. As next very important aspect comes the *particle image density*. It can be qualified in three types. By the low image density, images of individual particles can be identified. This kind of recordings are appropriate for Particle Tracking Velocimetry (PTV), where individual trajectories of single particles can be followed. In the case of medium image density, single particles can be distinguished as well but no image pairs can be identified with simple visual inspection. Thus the medium density images are evaluated with statistical techniques employed by the PIV. By the high image densities, the scattered light from single particles overlaps and no individual images can be detected [7].

The *spatial resolution* of the velocity map evaluated by a PIV system is determined by the size of the interrogation areas, which further determines the number of independent velocity vectors. The *temporal resolution* depends on the frequency of the laser pulses and the camera. PIV is usually known for its high spatial resolution and not so good temporal one [7].

Since the exact information about the velocity fields is dependent mostly on the processing and post-processing of the PIV recordings it can be stated that PIV allows *repeatability of evaluation*. Thus, it is

possible to evaluate the recordings with different techniques without repeating the whole experiment [7].

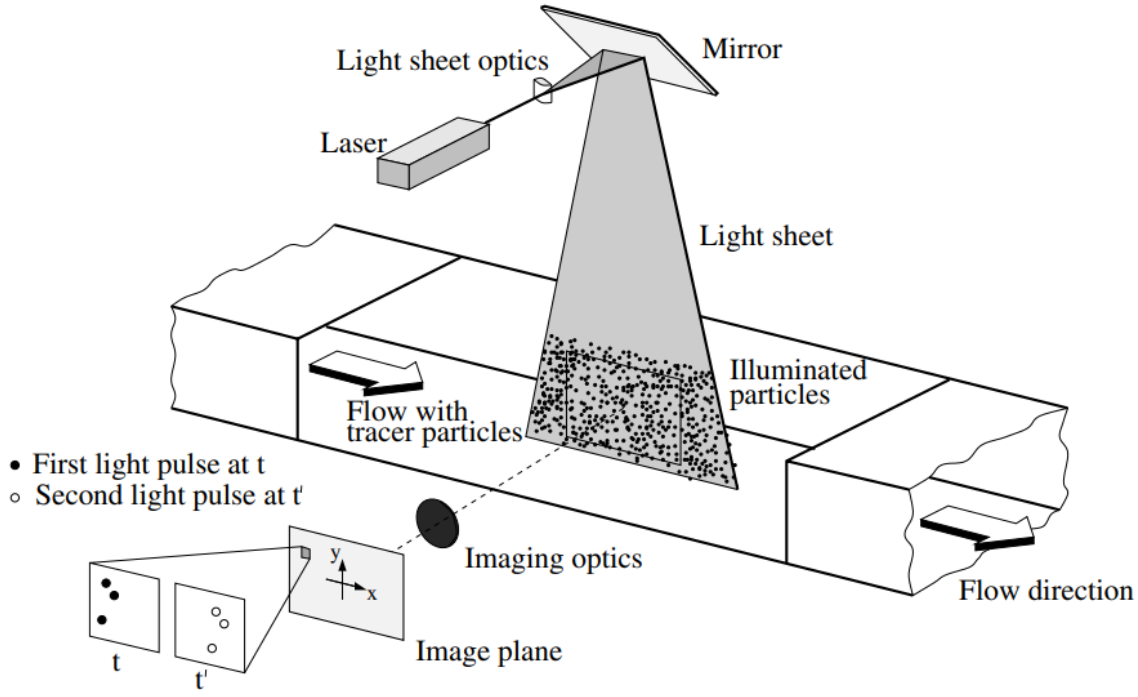

Figure 3.2 General arrangement of PIV system. From [7].

3.3. Working principle

As it can be observed from the typical PIV arrangement in figure 3.2, a thin light sheet within the flow is illuminated with two pulses of a laser. The time delay between the pulses is adjusted to the flow velocity and the magnification of the imaging optics. Making the assumption that the tracer particles move with the local flow velocity, a local displacement vector is evaluated from a digital recording of the light scattered by the tracer particles by the means of a single or a sequence of frames. The evaluation process is done by dividing of the frame in small regions called "interrogation areas" where the particles are assumed to move homogeneously between two illuminations, thus the distance travelled by them for that time is estimated for each interrogation area with the help of auto- and cross-correlation functions [7].

3.3.1.Setup

Experimental PIV setup usually comprises the assembly of several sub-systems most of which are depicted on figure 3.2. However, there are some more specific applications of PIV, which include some additional devices.

First part of the setup that will be discussed are the *tracer particles* (also referred to as seeding particles). As it was outlined earlier, the fluid velocity is not directly measured but evaluated from the particle velocity. If there is a discrepancy between the density of the fluid and the density of the particles, this usually results in a velocity lag [7]. A reliable prediction about the behaviour of the particles can be obtained from the Stokes number (St), which is the ratio between the characteristic time of a particle to the characteristic time of the flow:

$$St = \frac{\tau_s \, u_f}{l_f} \tag{8}$$

where u_f is the fluid flow velocity, l_f is the flow characteristic length (e.g. hydraulic diameter) and τ_s is the relaxation time of the particle derived from the Stokes' drag law for a continuously accelerating fluid assuming spherical particles:

$$\tau_s = \frac{d_p^2 \, \rho_p}{18\mu} \tag{9}$$

where d_p is the particle diameter, ρ_p is the density of the particle and μ is the fluid dynamic viscosity. It is considered that a lower Stokes number represent a better tracing accuracy. At $Stk \ll 1$, the particles are supposed to follow the streamlines of the fluids with good fidelity and if $Stk < 0.1$, the tracing accuracy becomes 99% and higher. At $Stk \gg 1$, the particles do not follow the flow anymore [50].

In some flows a natural seeding is available in the meaning of naturally occurring particles visible enough to act as tracers for PIV. In all other cases, an addition of appropriate particles is needed. In table 3.1 are listed some of the typical tracing particles for liquid flows [7]. Seeding of the fluid could be particularly hard considering gases, but since the focus of this study is on liquid flows, where the tracer particle can be easily suspended in the fluid before the start of the experiment, this topic is not going to be discussed in a detail.

Table 3.1 Classification of tracer particles for liquid flows. Adapted from [7]

Type	*Material*	*Diameter in μm*
Solid	Polystyrene	1-100
	Aluminum flakes	2-7
	Hollow glass spheres	10-100
	Granules for synthetic coatings	10-500
Liquid	Different oils	50-500
Gaseous	Oxygen bubbles	50-1000

Next part of the setup is the *light source*. Lasers have the most merit to the PIV, since they are able to emit a monochromatic light with a high energy density. With the help of an additional optical system the laser light can form a thin light sheet for particles illumination and recording with minimum chromatic aberrations. A laser setup consists generally of a laser material or an active medium, a source of pumping energy for excitation of the active medium and a resonator in the meaning of a system of mirrors arranged in way to induce an oscillation in the laser material. Lasers are classified by their material, which can be atomic or molecular gas, semiconductor or solid [7].

Regarding PIV use, the most popular choice are solid-state Neodym-YAG (Nd:YAG) lasers. They work with Nd^{3+} ions incorporated in YAG (yttrium-aluminum-garnet) crystals and are known for good thermal and mechanical properties. The pumping source can be a white light, which provides broad energy bands. The strongest emission of the Nd:YAG is at 1064 nm. With the design of the laser cavity (because of its influence on the population inversion in the active medium, and therefore emission) and pump pulse of a flash lamp, many laser pulses can be achieved. Additionally, a quality switch (Q-switch) can be implement inside the cavity, allowing the cavity to resonate at the point with highest energy during the flash lamp cycle with a very powerful laser pulse as an output. Many giant pulses out of one resonator is of a great interest for PIV. Another interesting laser feature in that sense, except for the Q-switch, is the double oscillator. It gives the ability to the operator to choose the time between the two illuminations independent on the pulse strength. This includes a linear polarisation of the beam of Q-switch laser and further its wavelength is "frequency-doubled" with the use of a second harmonic generator (SHG), which is a non-linear crystal. Frequency-doubling in its principle is a conversion of the 1064 nm wavelength of the originally emitted infrared light into 532 nm wavelength, i.e. visible

green light. Around one third of the initial light energy is available after the frequency-doubling [7]. Some of the more important features of an Nd:YAG PIV-laser system are outlined in Table 3.2:

Table 3.2 Properties of Nd:YAG PIV-laser systems. Adapted from [7].

Repetition rate	10Hz
Pulse energy for each of two pulses	320 mJ
Roundness at 0.5 m and at 8 m from laser output	75%
Spatial intensity distribution at 0.5 m and at 8 m from laser output	< 0.2
Deviation from collinearity of laser beams	< 0.1 mm/m
Beam diameter at laser output	9 mm
Delay between two laser pulses	0 to 10 ms
Resolution	5 ps
Working temperatures	15º-35º C
Power requirements	220-240V, 50 Hz

This section will review the specifics of the *flow illumination*. In conventional PIV there is a typical approach of generation of a thin light sheet with the help of different lens configurations. However, in the case of micro-flows such configurations cause significant diffraction and usually restrict the optical access. The solution in this situation is volume illumination of the flow. In practice the tracing particles are visualized with optics with depth of field either greater or smaller than the depth of the flow of interest. In the first case, when the depth of field is larger, all the particles in the field of view are with a suitable focus and approximately equal contribution to the correlation function. This results in lack of velocity distribution along the depth of the flow, e.g. in a pressure driven flow the particles around the centre are supposed to move faster, whereas these near the walls move slower. However, if they are all in focus a weighted-average velocity profile will be obtained instead of parabolic one. The case of depth of field smaller than the depth of the flow is schematically shown on figure 3.3. The idea is that the optical system (usually the objective of a microscope) focuses only the particles within a domain with thickness δ also known as a depth of correlation (z_{corr}) and all the particles out of this domain remain unfocused which causes a background noise. The difference between the depth of field and the depth of correlation is that the former stands for the disaffection of the image focus from the displacement of the light source relatively to focal plane and the latter is a measure of the distance from the focal plane in which a particle is focused sharp enough to contribute to the correlation function. It is obvious that the particle size is important to determine the depth of correlation, whereas it does not matter for the depth of field [7], [51], [52].

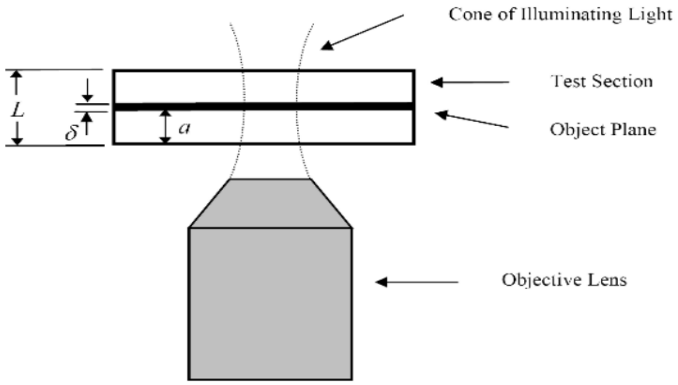

Figure 3.3 Arrangement of volume illumination in PIV, where the light is coming out microscope objective lens and the depth of field is smaller than depth of the flow, where L is the height of the test section, a is the distance between the object plane and the border of the test section and δ is the depth of field. . From [51].

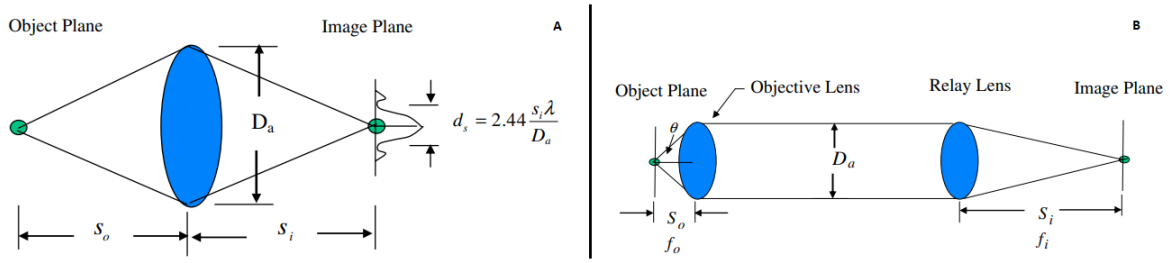

Figure 3.4 A Single-lens macroscopic system and B Infinity-correlated optical system usually used in microscopes, consisting of objective lens and a relay lens with much larger focal length for high magnification. Adapted from [53].

Important aspect in the investigation of micro-flows is the *microscopic imaging*. Microscopes are used to magnify images employing several lenses, which are located in the objective and in the eyepiece. The product of the respective object magnification and eyepiece magnification represents the total magnification of a microscope. Moreover, the objective usually provides the illumination in microscopy, in the meaning of transmitted, reflected or fluorescent light. In this sense, it is important to mention that the objective determines the quality of the picture. Common aberrations for the objective lenses are spherical, chromatic, curvature of field, chromatic and astigmatic. A parameter that determines the resolution of the microscope along with its ability to gather light is the numerical aperture of the objective. The other important factor for the resolution is the substage condenser, which assures that the illumination of the object of interest is with uniform intensity over the entire field of view. The condenser achieves this by concentrating the light from the source into a cone of light [7].

Furthermore, to discuss the spatial resolution of microscopic imaging, some general limitation factors should be considered. Particularly, interesting for PIV is the diffraction limited imaging. The problem with the resolution comes from the fact that if a distant point source is imaged, even by lens without any aberrations, the image does not appear like a point but form a Fraunhofer diffraction pattern [54]. With the use of the Fraunhofer approximation for far fields, it can be shown that the resulting diffraction pattern, also known as Airy disk for low exposure and Airy rings for high exposure, represents the Fourier transform of the aperture's transmissivity distribution [7], [55]. The relationship between the width of the Airy function d_s and the aperture diameter is given by the formula (see Figure 3.4 A) [53]:

$$d_s = 2.44\frac{s_i\lambda}{D_a} \tag{10}$$

where s_i is the distance between the lens, λ is the wavelength of the light and the object of imaging and D_a is the diameter of the lens aperture. From (7) it is already clear that with a larger aperture and closer distance between the lens and the imaged object the resolution of the image is increasing.

For an exact estimation of the diffraction limited spot size in a single-lens macroscopic system a definition for f-number should be given in the form of $f^{\#} = \frac{f}{D_a}$ and the following representation of s_i should be considered[53]:

$$s_i = (M+1)f \tag{11}$$

where M is the magnification and f the focal length of the system. The combination of (10) and (11) together with $f^{\#}$ leads to the expression for a diffraction limited spot size defined by Adrian and Yao [56]:

$$D_{Sp} = 2.44(M+1)\lambda f^{\#} \tag{12}$$

Figure 3.5 A Single frame/multi exposure mode and B Multi frame/single exposure mode. Adapted from [7].

When it comes to an infinity-corrected lens systems, as in the microscopes (see figure 3.4 B), first an expression for numerical aperture should be given as $NA = n\ sin\theta$, where n is the refraction index of the medium of interest and θ is the half-angle of the light subtended by the objective lens. For PIV systems is useful to assume the air as medium of immersion and small numerical apertures. In this way the following reduced formulation for the f-number can be used - $f^{\#} = \frac{1}{2\ NA}$ [7], [53], [57]. Combining this formulation with (12) leads to a diffraction limited spot size directly related to the numerical aperture [53]:

$$D_{Sp} = \frac{1.22(M+1)\lambda}{NA} \tag{13}$$

As a last part of the setup *recording methods and techniques* will be discussed. In general, recording with respect to PIV is divided into two main branches called single frame/multi exposure PIV and multi frame/single exposure PIV (see Figure 3.5 A and B). The former one refers to recording the illuminated flow on a single frame and the latter captures an image for every illumination pulse. The single frame/multi exposure method is historically the first one to be used in a combination with photography. However, it does not store information about the temporal order of the illumination pulse, which results in directional ambiguity of the displacement vector, which makes the evaluation much more complex requiring additional schemes to resolve this ambiguity. On the other hand, the multi frame/single exposure approach retains the temporal order of the recordings and is much easier form in terms of evaluation, therefore it is preferable and widely used after the technological advances in the digital capturing [7].

In terms of technology, both analogue and digital solutions have been employed for a PIV use. Because of the wide availability of digital image recording technique and the obvious advantages compared to the photographic methods, especially regarding to the PIV use, the focus in this section will stay on digital recording, whereas analogue techniques will not be discussed.

The most common electronic sensors used for PIV image recording are based on either on charge coupled device (CCD) technology or complementary metal-oxide-semiconductor (CMOS) technology. A CCD element works on the principle of the photoelectric effect meaning that when a light photon hits the material of the element it induces emission of electrons. By continuous exposure to light electrons are accumulated and the CCD element stores them in the same way as in a capacitor. A single CCD element, also called pixel, has a limited capacity for electron storage which is usually between 10^4 and 10^5 electrons. By overexposure this number is exceeded causing the electrons to migrate to the neighbouring pixels and resulting in a blooming image. Typical size of a pixel is around 10×10 µm or roughly 100 pixels per mm. The principle behind the individual pixel in the CMOS technology is the same as in the CCD. The main difference between the CCD and the CMOS sensors comes from the MOS-FET (metal-oxide semiconductor field-effective transistors) technology implemented in the CMOS elements, which gives a direct access to every photodiode in the array. Linking an individual circuit to every photo-element together with the individual control leads to significant advantages like integrating amplifiers, non-linear signal transformation and higher framing rates. However, the integration of a circuit of every single pixel results in two major drawbacks. The first one is the noise

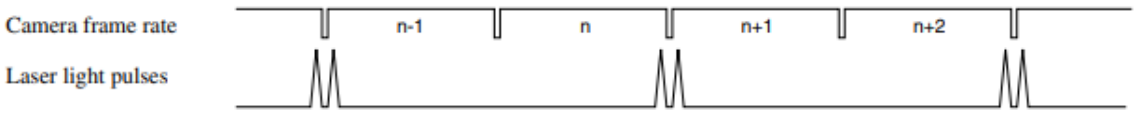

Figure 3.6 Timing diagram of a PIV recording. Adapted from [7].

from the variations in the output of the individual circuits across the array, thus the larger sensors, which are usually used for PIV, yield greater noise. The second problem comes from the limited area for the photo-elements used for integrating circuits. This decreases the electron storage capacity and results in lower sensitivity of the sensor [7], [58]. There are many more details regarding the technical restrictions of CCD and CMOS sensors and the invented solutions to these problems. However, their discussion is not an object of this work.

Important for the modern PIV setups are digital cameras with frame rates matching repetition rates of a flash lamp pumped double oscillator Nd:YAG laser. This can be accomplished with the available CCD and CMOS cameras. Typical CCD architecture that allows two PIV recordings separated in time by the means of microseconds are the full-frame interline transfer CCD. It is based on the principle of the interline transfer CCD sensor, which includes an additional vertical transfer registers incorporated between the active pixels. While by the classic interline transfer CCD two vertically adjacent pixels share a common storage space in the register in the full-frame derivative every each active pixel has its own storage site. Charges from the light sensitive area are transferred to the masked storage areas for less than a μs. This results in a high camera frame rate that made the single exposure/double frame PIV mode possible. Specifically for a pulse delay of 1 μs the PIV image frame rate will be equal to the half of the camera frame rate as it is shown on the timing diagram on Figure 3.6. Moreover, the commercially available high-speed CCD cameras are with frame rate of 1000/s at resolutions of 512×512 pixels[7].

Because of the parallel architecture of the CMOS sensors, discussed earlier, which permits more output channels and thus faster pixel read out, the CMOS cameras are considered more advanced for a high-speed PIV application. Furthermore, the individual access to the elements in the array allows custom manipulation of the read out and the use of techniques like windowing, which is approach for reading smaller sub windows of the light active area of the CMOS sensor, resulting in faster frame rates with a lower image resolution. The high-speed CMOS cameras available on the market include such with frame rates of 3000/s at full megapixel resolution and even reaching 10 000/s when the resolution goes down to 512×512 pixels. This significant time resolution comes on the cost of a very large data production. To overcome this obstacle many cameras are equipped with up to 16 GB inbuilt memory.

3.3.2.Mathematical background and evaluation methods

For the purpose of evaluation, a digital PIV recording is divided into interrogation areas, also known as interrogation windows. The back-projection of these areas into the light sheet are called interrogation volumes and two such volumes employed for statistical evaluation comprise the measurement volume. Considering a single exposure, the random distribution of particle images corresponding to N tracer particles inside the flow is described by $\Gamma = \begin{pmatrix} \mathrm{X}_1 \\ \vdots \\ \mathrm{X}_\mathrm{N} \end{pmatrix}$ as a state of the ensemble at given time t, where $\mathrm{X}_\mathrm{i} = \begin{pmatrix} X_i \\ Y_i \\ Z_i \end{pmatrix}$ is representing the position vector of the tracer particle i in a 3N-dimensional space. The particle position and the image position are related by the expressions $\mathrm{X}_\mathrm{i} = \mathrm{x}_\mathrm{i}/M$ and $\mathrm{Y}_\mathrm{i} = \mathrm{y}_\mathrm{i}/M$, where the lower case letters refer to the coordinates in the image plane such that $\mathrm{x} = \begin{pmatrix} x \\ y \end{pmatrix}$ is the image position vector and M is the constant magnification factor [7], [59]. Furthermore, it is believed that an image is best described by the convolution of the geometrical image and the impulse response of the imaging

system. This is usually represented as the image intensity distribution. In order to obtain expression for this, the image impulse response is defined as a point spread function or in the case of PIV images, specifically, as the aforementioned Airy function, which is Gausian with respect to x and y and will be referred as to $\tau(\mathrm{x})$. The point spread function is considered to be different for particles on different positions. It can be assumed that the scattering properties and the sensor sensitivity are constant over the plane, so the parameter that remains dependent on the position is the image intensity. The intensity can be weighted with the help of the so called transfer function which expresses the conversion of the light energy of a particle i from the interrogation volume V_I into an electronic signal and is given by $V_0 = W_0(X,Y)\, I_0(Z)$, where $W_0(X,Y)$ is the interrogation window function geometrically back projected into the light sheet and $I_0(Z)$ is the intensity profile of the laser light sheet in Z direction. Furthermore, to relate $\tau(\mathrm{x})$ to the geometrical part of the particle image we use the Dirac delta-function for shift to position $\mathrm{x_i}$ as it follows: $\tau(\mathrm{x}) * \delta(\mathrm{x} - \mathrm{x_i}) = \tau(\mathrm{x} - \mathrm{x_i})$. With the assumption that the considered particle images do not overlap we can express the intensity distribution as [7]:

$$I(\mathrm{x}, \Gamma) = \sum_{i=1}^{N} V_0(X_\mathrm{i})\, \tau(\mathrm{x} - \mathrm{x_i}) \tag{14}$$

With this expression we can determine spatial estimators for the mean value and the variance of the intensity distribution of the image. Moreover, the mean value of the intensity field is approximated as:

$$\mu_\mathrm{I} = \langle I(\mathrm{x}, \Gamma) \rangle = \frac{1}{a_\mathrm{I}} \sum_{i=1}^{N} V_0(X_\mathrm{i}) \int_{a_\mathrm{I}} \tau(\mathrm{x} - \mathrm{x_i})\, dx \tag{15}$$

where a_I is the interrogation area. Therefore, the auto-correlation is given by:

$$\begin{aligned} R_\mathrm{I} = \langle I(\mathrm{x}, \Gamma), I(\mathrm{x} + \mathrm{s}, \Gamma) \rangle = \frac{1}{a_\mathrm{I}} \sum_{i \neq j}^{N} V_0(X_\mathrm{i}) V_0\big(X_\mathrm{j}\big) \int_{a_\mathrm{I}} \tau(\mathrm{x} - \mathrm{x_i})\, \tau\big(\mathrm{x} - \mathrm{x_j} + s\big)\, dx \\ + \frac{1}{a_\mathrm{I}} \sum_{i=j}^{N} {V_0}^2(X_\mathrm{i}) \int_{a_\mathrm{I}} \tau(\mathrm{x} - \mathrm{x_i})\, \tau\big(\mathrm{x} - \mathrm{x_j} + s\big)\, dx \end{aligned} \tag{16}$$

where s is the separation vector and the $i \neq j$ term represents the correlation of the different particle images, responsible for the noise, whereas the $i = j$ represents the correlation of an individual particle picture with itself.

Furthermore, for two singly exposed recordings with time of the second exposure $t' = t + \Delta t$, where t is the time of the first exposure, we can assume a constant displacement D for all particles within the interrogation volume, expressed as $\mathrm{X_i'} = X_\mathrm{i} + D = \begin{pmatrix} X_i + D_X \\ Y_i + D_Y \\ Z_i + D_Z \end{pmatrix}$ and respectively the displacement of the particle image on the image plane is defined as $\mathrm{d} = \begin{pmatrix} MD_X \\ MD_Y \end{pmatrix}$. With these definitions together with the assumptions that the light sheet and the window properties are the same for the both exposures a cross-correlation function of the two interrogation areas is derived as [7]:

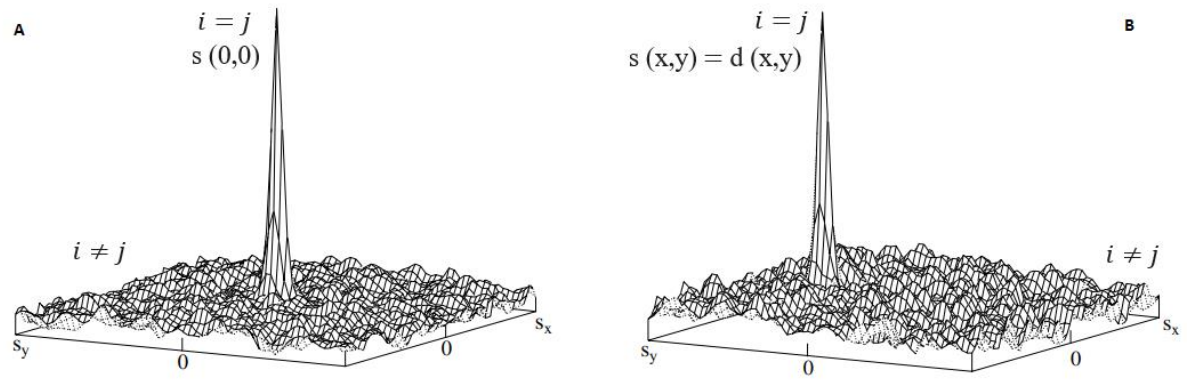

Figure 3.7 A Distributions of peaks in auto-correlation function and B distributions of peaks in cross-correlation function. Adapted from [7].

$$R_{\mathrm{II}}(s,\Gamma,D) = \frac{1}{a_{\mathrm{I}}}\sum_{i,j} V_0(X_{\mathrm{i}})V_0\left(X_{\mathrm{j}}+D\right)\int_{a_{\mathrm{I}}} \tau(\mathrm{x}-\mathrm{x_i})\,\tau\left(\mathrm{x}-\mathrm{x_j}+s-d\right)dx \tag{17}$$

Analogically to (16), (17) can be decomposed into a part for $i \neq j$ terms, responsible for the noise in the correlation plane, and a part for $i = j$, containing the displacement information. Moreover, it can be proven that the autocorrelation peak, at its maximum, is located at the separation vector $|\mathrm{s}| = 0$ (see fig. 3.7 A). Therefore the displacement correlation peak reaches its maximum at $\mathrm{s} = \mathrm{d}$ (see fig. 3.7 B) so we can say that the location of this maximum contains the information of the average in-plane displacement, and thus the two-dimensional velocity components [7].

In digital PIV evaluation, rather numerical approach is used than analytical. In order to understand the direct implementation of the cross-correlation function in the evaluation process we can simplify (17) to:

$$R_{\mathrm{II}}(x,y) = \sum_{i=1}^{p}\sum_{j=1}^{q} I(i,j)I'(i+x,j+y) \tag{18}$$

where I and I' are the grey value distributions within the interrogation areas with dimeson $p \times q$ pixels of the first and the second image respectively. In general, the first image is overlapped with the second at different positions. The first image is shifted only by linear translation and certain degree of overlapping is considered (usually 50% [24], [43], [44]). At every position (x, y) the sum of the products of all overlapping pixel intensities produces one cross-correlation value $R_{\mathrm{II}}(x, y)$. At the position where R_{II} is at its maximum, the sum of the product of the pixel intensities is the highest, meaning that the particle images have matched. The displacement can be estimated by comparison between the position of the maximum cross-correlation and the original position of the first image, analogically to Figure 3.7B. The consequence of this approach is that the multiplications increase with the size of the interrogation window, and only first order vectors can be revealed from the linear translations of the images of the particles. This means that an expansion of the area of the window leads to quadratic increase of the multiplications resulting in considerable computational cost [7].

Another, more favorable approach is the frequency domain based correlation. It is based on the theorem stating that the cross-correlation of two functions is equivalent to a complex conjugate multiplication of their Fourier transforms:

$$R_{\mathrm{II}} \Leftrightarrow \hat{I}\cdot\hat{I}'^{*} \tag{19}$$

where $\hat{I}$ and $\hat{I}'$ represent the Fourier transforms of I and I', respectively. Moreover, for discrete data Fourier transform can be implemented as fast Fourier transform (FFT). For two-dimensional correlation the number of computational operations reduces from $O[N^4]$ to $O[N^2 log_2 N]$ [7].

The use of FFT is related to limitations and effects like fixed sample sizes, periodicity of data, aliasing, limited displacement range, and bias error. This issues lead to altering of the correlation signal and unrealistic results. To cope with those problems, along with other general noise sources, there are some correlation signal enhancement techniques established.

Partially, the signal can be increased with pre-processing of the pictures. One of the pre-processing methods employs background subtraction, which removes some of the stationary image artefacts. Other methods are based on filtering. For instance high-pass filter can be used for cutting low-frequency background noise and leave the particle images unaffected, or a narrow-banded low-pass filter can be suitable for removing high-frequency camera shot noise. A very useful method for adjusting the image contrast is the min/max filter approach, which consists of computing envelopes with local minimum and maximum intensities and later normalizing every pixel with the local values in the envelopes.

Furthermore, processing takes place. In that sense, a wide spread approach for micro-PIV is the ensemble correlation. In general, it averages the coincident correlation planes of sequence of images, instead of collecting data about the displacement of every individual image pair. This approach is beneficial because it reduces the noise due to Brownian motion, typical for microflows. However, all the information regarding the flow steadiness is lost. Moreover, not only the correlation signal can be enhanced but also the interrogation algorithms can be improved. A popular approach in that sense is the image deformation technique. For the use of the cross-correlation function, an assumption is made, that the particles move uniformly within the interrogation area, which is not the case in reality. This issue is overcome with deformation of the window, according to the local velocity gradient. Analogically, the scheme is applied over the whole PIV image. The result is a decrease in the in-plane loss of pairs, more accurate peak shape, and approximately double spatial resolution compared to the one obtained with a standard interrogation [7].

In order to obtain meaningful velocity fields, the raw data should be post-processed. Considering PIV, post-processing consist of several actions. A *validation of raw data* is important for removing the incorrect velocity vectors. There are many established algorithms, which can work fast over big amounts of data. Such is the global histogram operator - a simple algorithm for removing velocity outliers above curtain threshold. The dynamic mean value operator is testing each velocity vector by comparing its magnitude to an average value of its nearest neighbours [7]. Median test is filtering velocity vectors by sorting, linearly, neighbouring vectors (with respect to magnitude or U/V component) and comparing the difference between the median and the tested vector to a certain threshold [60]. Furthermore, the data can be post-processed by filling in missing values. A popular replacement scheme is a bilinear interpolation.

Since the purpose of a flow investigation is rarely only a detailed map of the velocity field, there are ways to extract more differential and integral quantities in the meaning of post-processing of the velocity field. Of a particular interest are the differential quantities, which can be obtained by building the deformation tensor from the velocity data and decomposing it into symmetric and antisymmetric part:

$$\frac{\mathrm{dU}}{\mathrm{dX}} = \begin{bmatrix} \frac{\partial U}{\partial X} & \frac{1}{2}\left(\frac{\partial V}{\partial X}+\frac{\partial U}{\partial Y}\right) & \frac{1}{2}\left(\frac{\partial W}{\partial X}+\frac{\partial U}{\partial Z}\right) \\ \frac{1}{2}\left(\frac{\partial U}{\partial Y}+\frac{\partial V}{\partial X}\right) & \frac{\partial V}{\partial Y} & \frac{1}{2}\left(\frac{\partial W}{\partial Y}+\frac{\partial V}{\partial Z}\right) \\ \frac{1}{2}\left(\frac{\partial U}{\partial Z}+\frac{\partial W}{\partial X}\right) & \frac{1}{2}\left(\frac{\partial V}{\partial Z}+\frac{\partial W}{\partial Y}\right) & \frac{\partial W}{\partial X} \end{bmatrix} + \begin{bmatrix} 0 & \frac{1}{2}\left(\frac{\partial V}{\partial X}-\frac{\partial U}{\partial Y}\right) & \frac{1}{2}\left(\frac{\partial W}{\partial X}-\frac{\partial U}{\partial Z}\right) \\ \frac{1}{2}\left(\frac{\partial U}{\partial Y}-\frac{\partial V}{\partial X}\right) & 0 & \frac{1}{2}\left(\frac{\partial W}{\partial Y}-\frac{\partial V}{\partial Z}\right) \\ \frac{1}{2}\left(\frac{\partial U}{\partial Z}-\frac{\partial W}{\partial X}\right) & \frac{1}{2}\left(\frac{\partial V}{\partial Z}-\frac{\partial W}{\partial Y}\right) & 0 \end{bmatrix} \tag{20}$$

where the diagonal and off-diagonal parts of the symmetric part represent respectively elongation strains and the shear strains, and the antisymmetric part express components of the vorticity. Therefore, for a conventional two-dimensional PIV, where the obtained velocity data is restricted only to U and V components and can be differentiated only in X and Y directions, only the vorticity component normal to the plane of investigation can be derived from the deformation tensor. Elongation and shear strains are only available in-plane. If we assume an incompressible fluid, where $\nabla \cdot U = 0$ out-of-plane elongation can be estimated as $\frac{\partial W}{\partial X} = -\frac{\partial U}{\partial X} - \frac{\partial V}{\partial Y}$ [7]. From those quantities further can be estimated the rate of strain and respectively the viscous shear stress, which for Newtonian fluids holds the following relationship with the strain rate:

$$\dot{\varepsilon} = E\mu \tag{21}$$

where $\dot{\varepsilon}$ is the strain rate, E is the viscous shear stress and μ is the dynamic viscosity of the fluid.

As stated earlier, integral quantities like circulation and mass flow can be estimated as well. However, they are not object of this work and their calculations will not be discussed in details.

3.3.3.Noise and accuracy

Most of the sources of noise induced by the setup were described in section 3.3.1. A suitable measure of the effect of the noise on the accuracy of the evaluated results is the signal-to-noise ratio (SNR). SNR, in the meaning of a volume-illuminated two-dimensional PIV, is defined by Mainhart et al. [51] as the peak image intensity divided by the average background intensity. The higher the SNR, the better the accuracy of the measurement. Important parameters affecting the SNR are the test-section geometry, particle size, illumination, recording optics, seeding density, etc. Because of the volume illumination, all the particles contribute to the intensity of the image. The focused particles are those situated in the depth of correlation, defined earlier (see Figure 3.3). Furthermore, Mainhart et al. [51] relates the thickness of the in-focus plane to the particle size, diffraction, illumination and recording optics with the expression:

$$\delta z_{corr} = \frac{3n\lambda_0}{NA^2} + \frac{2.16\, d_p}{\tan\theta} + d_p \tag{22}$$

where δz_{corr} is the depth of correlation, n is the refractive index of the imaging medium, λ_0 is the wavelength of light in vacuum, NA is the numerical aperture of the objective lens, θ is the collection angle of the objective and d_p is the dimeter of a tracer particle. All the particles out of the plane with thickness δz_{corr} are considered out-of-focus and increase the average background intensity, which results in lower SNR. Therefore, a test-section with a smaller depth will increase the SNR at fixed particle concentration, and analogically lower seeding density is beneficial for the SNR at fixed height of the geometry of interest (See table 3.3) [51].

Table 3.3 Experimental SNR values for various particle concentrations and test-section depths. The relatively low values are consequence of the small diameter of the tracer particles used for this experiment (d_p=200 nm). From [51].

Test-section depth (μm)	**Particle concentration (by volume)**			
	0.01%	**0.02%**	**0.04%**	**0.08%**
25	2.2	2.1	2.0	1.9
50	1.9	1.7	1.4	1.2
125	1.5	1.4	1.2	1.1
170	1.3	1.2	1.1	1.0

4. Computational fluid dynamics (CFD)

Computational Fluid Dynamics (CFD) is the simulation of fluid flow, based on the numerical solution of a set of partial differential equations on a finite volume grid. CFD can be a powerful tool in the research of fluid flows. However, due to their complex nature and limited computational power, the interpretation of CFD results must be handled with a great care. Experimental data, such as the presented micro-PIV measurements, aid in the validation of these numerical methods.

The following description of the CFD principle and methodology is based on the book Computational Fluid Dynamics: Principles and Applications by Jiri Blazek [62].

4.1. Methodology of CFD

Due to the variety of conditions characterizing a fluid, different methods for the derivation of a suitable solution exist. The methodology reviewed here considers an incompressible Newtonian fluid.

4.1.1.Governing equations

If we assume, that the flow comprises a continuum of infinitesimally small elements, its dynamical behaviour can be determined by the conservation laws (conservation of mass, conservation of momentum and conservation of energy). The net effect of an amount of quantity being transported across the boundary of an arbitrary volume, which amount is called a flux, characterizes the conservation of this quantity. The flux is separated into two parts – one due to convection and another due to molecular motion present in fluid at rest. In order to model the dynamic behaviour of the fluid, an arbitrary volume has to be defined. For this purpose the flow field is separated into a number of volumes called finite control volumes. Moreover, the dynamic behaviour of a fluid can be represented by the following expression relating all the aforementioned factors:

$$\frac{\partial}{\partial t}\int_{\Omega} \vec{W}\,\mathrm{d}\Omega + \oint_{\partial\Omega} (\vec{F}_{\mathrm{c}} - \vec{F}_{\mathrm{v}})\mathrm{dS} = \int_{\Omega} \vec{Q}\,\mathrm{d}\Omega \tag{23}$$

where $\vec{W}$ is the vector of conservative variables, $\vec{F}_{\mathrm{c}}$ is the vector of convective fluxes, $\vec{F}_{\mathrm{v}}$ is the vector of viscous fluxes and $\vec{Q}$ comprise all volume sources. This vectors are characterized by 5 unknowns, namely the u, v and w velocity components together with the pressure p and the enthalpy H. These unknowns are derived with a system of 5 equations of conservation. Furthermore, the solved vectors together with (23) build the *Navier-Stokes equations* which express the way in which mass, momentum and energy are exchanged through the boundary $\partial\Omega$ of a control volume Ω fixed in space.

4.1.2.Spatial discretization

Different schemes for a spatial discretization of the governing equations (23) exist, however they divide in three main categories: finite-difference, finite-volume, and finite-element. Any of these schemes use a grid in order to discretize the Navier-Stokes equations. Grids can be classified into structured and unstructured. By the structured grids every nod is specified by unique indexes i, j and k, and corresponding Cartesian coordinates $x_{i,j,k}, y_{i,j,k}$ and $z_{i,j,k}$ respectively, whereas by the unstructured nodes there is no particular order. Cells are quadrilaterals in 2D or hexahedra in 3D for the structured grids, and mix of quadrilaterals and triangles or mix of hexahedra, tetrahedral, prisms and pyramids respectively for the unstructured grids.

Of a specific interest for this work is the finite-volume discretization method. The Navier-Stokes equations are discretized directly in the physical space by dividing it into a number of arbitrary polyhedral control volumes. The quantity of the flux crossing an individual face of the control volume can be estimated with different approaches, which choice affects the accuracy of the spatial discretization. There are two general approaches based on the grid. The first one is called cell-centred

scheme, where the information about the flow quantities is located in the centre of the grid cell, respectively the control volume is matched completely with the grid cell. The second scheme is called cell-vertex, where the important information about the flow is stored in the grid point. In this case the control volume can be comprised of all cells connected to the specific point or just some predefined volume centred around this point.

4.1.3.Temporal discretization

Considering the governing equations (23) a temporal discretization can be obtained by writing a system of coupled ordinary differential equations in time for each control volume:

$$\frac{\mathrm{d}\left(\Omega \overline{M} \overrightarrow{W}\right)}{\mathrm{dt}} = -\vec{R} \tag{24}$$

where Ω is the control volume. For a static grid, Ω can be taken out of the derivative. $\vec{R}$ is called the residual and comprise the spatial discretization. Moreover, $\vec{R}$ is a non-linear function of the conservative variables $\overrightarrow{W}$. $\overline{M}$ is called the mass matrix and is a function of the grid that couples the system of differential equations. For steady-state cases $\overline{M}$ turns into the identity matrix and the system is decoupled. Moreover, the time derivative can be approximated by a non-linear scheme giving solution for the conservative variables in a time step manner with the help of the residual weighted at different time levels with the help of parameters. The accuracy of the scheme depends on the choice of parameters.

4.1.4.Initial and boundary conditions

In order to obtain a numerical solution for a flow simulation in space and time with the help of Navier-Stokes equations, we have to specify initial and boundary conditions. The initial conditions are responsible for the fluid description at the first time step. For an incompressible, laminar, internal flow, it is enough to prescribe the values for the pressure and the velocity. Furthermore, because of the division of the computational domain, some artificial boundaries are established, which means that the aforementioned physical quantities should be specified at this boundaries. The exact way of implementation of the boundary conditions in the flow solver has an effect on the accuracy of the solution, as well as on the robustness and the speed of convergence.

4.1.5.Turbulence

Turbulent flows possess features of interest to the CFD. Modelling turbulence, however, presents a significant problem, due to the required computational effort. Fortunately, the flows investigated in this work are kept strictly laminar (Re << 2300), therefore the presented simulations are modelled as laminar flows with very high accuracy.

III. Materials and Methods

5. Experimental setup

5.1. Working fluids

Due to the need of a transparent liquid for an implicit observation of the velocity field through the motion of fluorescent particles, it was chosen to dissolve the particles into two different fluids. Particles were dissolved into water and into a solution of xanthan gum (100 ppm) and sucrose (35%) in water as blood analogue with a viscosity comparable to this of the blood at different shear rates and a refractive index of 1.39 [63].

Rectangular channels are declared convenient for simulation of blood flow conditions due to the easily achievable laminar and thus axial flow in them [25]. For the purpose of this work 3 different rectangular channels (see fig. 5.1) were milled with a CNC milling machine from acrylic. After finalizing the details

within the flow volume, channels A and D were sealed by gluing a thin sheet of acrylic (refractive index $n = 1.49$) on the top of them, whereas by the others it was used microscope glass slide instead of acrylic (refractive index $n = 1.51$).

5.2. Flow channels

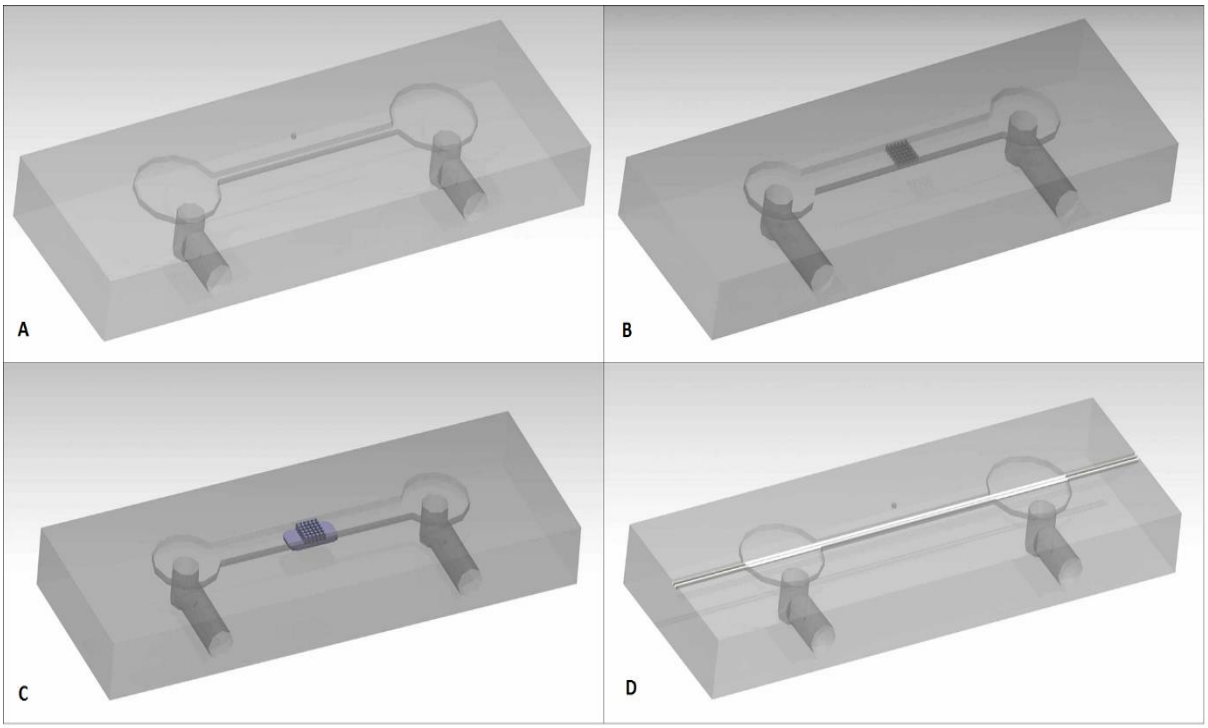

Figure 5.1 A. Rectangular channel, B. Channel milled rods, C. Channel with 3D printed rods, D. Channel with fibres.

5.2.1. Rectangular channel

Firstly, a channel with a simple rectangular profile was fabricated with 850 µm width and 800 µm height (see fig. 5.1A).

5.2.2. Channel with cylinder obstacles transverse to the flow (rods channel)

The idea behind the second channel is to include obstacles resembling fibres transverse to the flow. Two different designs were developed to fulfil the task. By the first one, an area of 6x6 cylindrical rods with a diameter of a fibre (400 µm) and distance of 600 µm between the centres of each 2 rods are milled directly with the CNC milling machine in the middle of the acrylic channel (see fig 5.1B). The channel profile dimensions are 3,8 mm in width and 1 mm in height. The latter one implicates a slot in the middle of the channel where a 3D print of the chosen obstacles is attached (see fig 5.1C). The second design promises fast changes of the obstacle composition. Unfortunately, due to the poor resolution of the 3D printer (Titan 1 Digital Light Processing 3D printer, Kudo 3D Inc., Dublin, CA, USA), the second design was impossible to accomplish.

5.2.3. Channel with fibres along the flow (fibre channel)

The third channel, visible in figure 5.1D, is again with a rectangular profile (1400 µm width and 800 µm depth) and involves the attachment of two polumethylpentene fibres (PMP 90/200, 3M Membrana OXYPLUS, 3M, Charlotte, NC, USA) parallel to the flow. The fibres outer diameter is 380 µm. The exact position of the fibres relative to the channel (see fig. 5.2) was measured later with the help of a digital microscope (Keyence VHX-5000 series, KEYENCE CORPORATION OF AMERICA, Itasca, IL, USA).

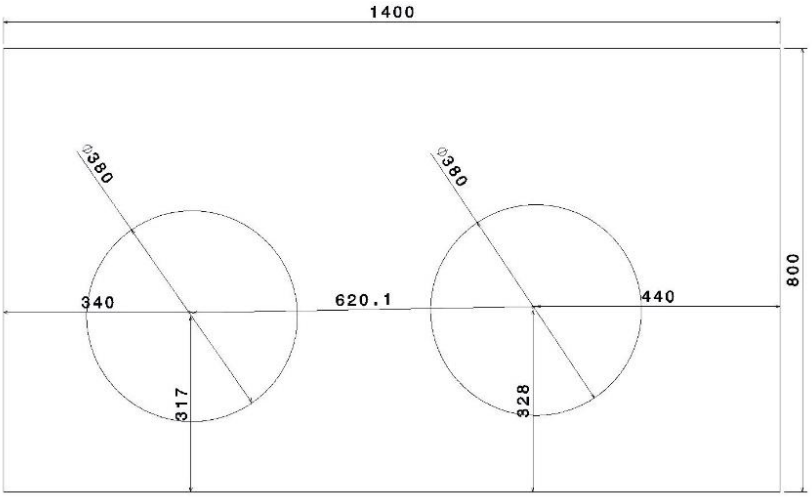

Figure 5.2 Drawing of the profile of the channel with fibres depicting the exact position of the fibres in the channel (dimensions in µm).

5.3. Micro-PIV system and settings

The system employed for micro-PIV measurements (see fig. 5.3) consisted of a Nd:YAG laser (Bernoulli 200-15, Litron Lasers Ltd., Rugby, Warwickshire, England) with emission at 532 nm in combination with an inverted microscope (Olympus IX73, Tokyo, Japan) and a high-speed camera (Zyla 5.5 sCMOS USB 3.0, Andor, Oxford Instruments plc, Tubney Woods, Abingdon, UK). The camera control input is connected to a synchronizer (LaserPulse Synchronizer 610036, TSI Inc., Shoreview, MN, USA), which adjusts the camera shots to the laser pulses. The output of the camera is connected to the control PC unit. The flow channel was fixed on the stage of the microscope and was connected to a syringe pump (Harvard Aparatus Model 11, Instech Laboratories, Inc, Plymouth Meeting, PA, USA), which ensured a range of flow rates for the different experiments.

The channel was illuminated by the laser beam coming from below the microscope stage through a dry 10× objective lens with a numerical aperture (NA) of 0.3. The beam path coming from the side of the microscope is pointed towards the objective lens with the help of dichroic mirror. The mirror reflects wavelengths up to 602 nm and passes all the wavelengths above, therefore with the camera placed behind the mirror, only an image of the excited particles on a dark background is acquired.

For seeding of the fluid two different types of tracer particles were used. The first type is a 2 µm in diameter polysterene particles with a density of 1060 kg/m^3, covered with a fluorescent dye with an excitation peak at 542 nm and emission at 612 nm (Fluoro-Max, Thermo Fisher Scientific, Fremont, CA, USA) which will be called Fluoro-Max. The second type is a 1.9 µm in diameter polysterene particles with a density of 1050 kg/m^3, covered with a fluorescent dye with an excitation peak at 530 nm and emission at 607 nm (FluoRot-Fi320, microParticles GmbH, Berlin, Germany) which will be called FluoRot.

The control of the system through the synchronizer and the image processing was accomplished with the 4G Insight software (4G Insight 11.1.0.5, TSI Inc., Shoreview, MN, USA). For the evaluation of the images first a pre-processing procedure was conducted. The procedure included subtraction of a preliminary taken background image and image filtering with a Gaussian low-pass filter. For the processing an ensemble PIV interrogation algorithm was employed, with the interrogation window changing with respect to the experiments. By the processing, additionally, was used image deformation technique. The cross-correlation function was evaluated using FFT, with the time between the images adjusted to the respective flow velocities for each experiment and with pass validation SNR of 1.5. Finally, the images were post-processed with local median validation test in a neighbourhood area of 5×5 interrogation windows. Further interpretation of the obtained vector fields was conducted in Tecplot 360 (Tecplot Inc., Bellevue, WA, USA).

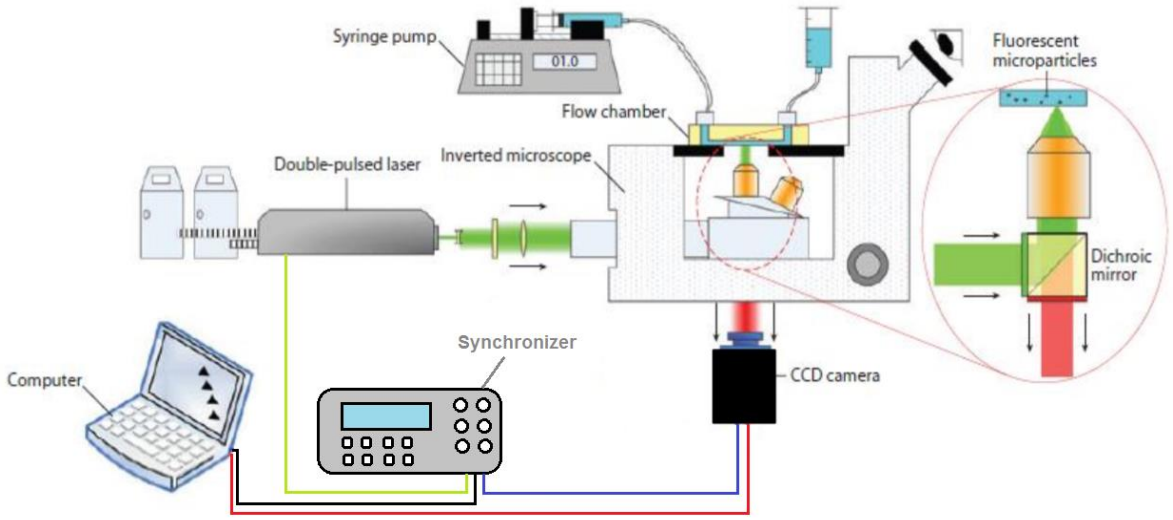

Figure 5.3 Experimental setup of the micro-PIV system.

6. CFD simulations

The numerical results presented in this work were performed by the open source software OpenFOAM® (Version 5.0). The numerical grids used for the simulations are obtained with the *blockMesh* and *snappyHexMesh* utilities. An incompressible, steady state solver (*simpleFoam*) was chosen for the solution of the governing equations. Post-processing of the results was conducted in the open source software ParaView (5.7.0).

The boundary conditions in all the cases are set in the following way – the inlet velocity is based on the velocity of the experiments, the pressure is set as arbitrary, since the simulation considers incompressible fluid, and the *no slip* condition is assigned to the walls.

6.1. Mean absolute percentage error (MAPE)

Estimation of the prediction accuracy of the CFD simulations is done by evaluating MAPE. It measures the deviation between the predicted values and the actual values of quantity of interest. It is given by the formula:

$$MAPE = \frac{1}{n}\sum_{i=1}^{n}\left|\frac{y_i - \hat{y}_i}{y_i}\right| \tag{25}$$

where y_i is the experimental value, $\hat{y}_i$ is the predicted value and n is the number of fitted points. The result from eq. 25 multiplied by 100 is the mean percentage error along the whole dataset.

7. List of experiments

7.1. Rectangular channel

In the first experiment it was chosen to use a simple channel geometry in order to create a highly reliable CFD simulation and easily compare it to micro-PIV results. The idea was to change different settings related to the experimental setup, such as:

- size of interrogation window – 64×64 and 64×16 pixels ;

- working fluid – water and blood analogue (water/sucrose/xanthan gum);

- seeding type – Fluoro-Max and FluoRot particles;

- seeding concentrations – 6.66% and 10% by volume;

- microscope focus – on 400 μm (middle) and 140 μm.

The experiments were conducted at a constant flow rate of 0.3 ml/min, with the microscope focused on 400 μm height – the middle plane of the channel (except for the last experiment). The time between two frames is 400ms.

Furthermore, the results of the different experiments were evaluated by choosing velocity profiles of interest and comparing them to the respective profiles from the CFD simulations. The MAPE was estimated in a reverse manner – how much the experimental value deviates from the predicted. For this purpose (25) is modified to:

$$MAPE = \frac{1}{n}\sum_{i=1}^{n}\left|\frac{y_i - \hat{y}_i}{\hat{y}_i}\right| \tag{26}$$

The Stokes numbers for the different particles in the different fluids were also evaluated together with the Reynolds numbers for the both working fluids (see table 7.1).

.

Table 7.1 Stokes and Reynolds numbers for the rectangular channel experiment.

	St		Re	
Seeding particles	Water	Blood analogue	Water	Blood analogue
Fluoro-Max	4.73×10^{-6}	1.48×10^{-6}	44.8	14.93
FluoRot	4.23×10^{-6}	1.32×10^{-6}		

7.2. Rods channel

The second experiment has to resemble the transverse flow through a package of fibres. The fibres are represented by acrylic, cylindrical rods (400 μm diameter) ordered in a square formation. The microscope was focused on the middle (500 μm height) plane parallel to the top/bottom plane. The flow was observed in between two single rods at 4 different pump rates –1.29, 2.57, 3.9 and 5 ml/min with both working fluids. Next, the results for the whole velocity fields and the velocity profiles right in between the rods were compared with CFD simulations. Both working fluids were simulated in the meaning of their different viscosities and at inlet velocities corresponding to 1.29, 2.57, 3.9 and 5 ml/min flow rates. To ensure that the velocity profile data sampled from the experiment correspond to the same position as the data from the CFD, an image processing function was developed in Matlab (MATLAB 2019R, The Mathworks Inc., Natick, MA, USA). The function returns the position of the rods in the image in the form of coordinates (in pixels) of the centre and the radius of the rods. Once, this coordinates are known, it is easy to obtain the respective data of interest.

Furthermore, Tecplot 360 offers the ability to evaluate the rate of strain in the field of interest. Knowing that the strain rate for an incompressible fluid is equivalent to the shear rate and assuming Newtonian fluid we can derive the shear stress on the fluid with the relationship $\tau = \dot{\gamma}\mu$, where τ is the shear stress, $\dot{\gamma}$ is the shear rate and μ is the dynamic viscosity of the fluid. Using again the aforementioned Matlab function we can obtain the data for the shear stress only between the two rods. Moreover, from Tecplot 360 can be exported detailed data about the streamlines in the region of interest, including the position in the plane and the velocity of the points of the streamline. Having this data, an estimation for the average residence time between the rods can be obtained. Using the experimental values for the shear stress and the residence time in equation (7), the hemolysis in between a single pair of rods was evaluated

for the 6 different flow rates – 0.43, 0.72, 1.29, 2.57, 3.9 and 5 ml/min, using the blood analogue fluid. The values for the hemolysis are obtained utilizing the Giersiepen-Wurzinger parameters.

To give a completed view of the processes with regard to the blood oxygenation membranes, a theoretical estimation of the Sherwood number (Sh) was derived. Sh was estimated with Reynolds numbers (Re) and the Schmidt numbers (Sc) derived for the respective channel geometry, fluid properties, and flow velocities corresponding to the 6 flow rates used for the derivation of the hemolysis index. Furthermore, the numbers were weighted with the coefficients proposed by Low et al. [64]. More specifically, the modification of (4) for CO_2 transport in blood transverse flow past square arrangement of cylinders was used:

$$Sh = 0.3838\varepsilon^{-0.611} Re^{0.2676\varepsilon^{-0.055}} Sc^{0.33} \tag{27}$$

where $\varepsilon = 0.5$ is the porosity of the PMP fibres. For characteristic length in Re was used the diameter of the fibres and Sc was estimated with the effective diffusion coefficient of CO_2 in blood $D_{effCO_2} = 1.25 \times 10^{-9}$ m^2/s. Both were estimated with a kinematic viscosity $\nu = 3 \times 10^{-6}$ m^2/s.

The Stokes and Reynolds numbers for the different fluids at the different flow rates were evaluated (see table 7.2).

Table 7.2 Stokes and Reynolds numbers for the rods channel experiment

	St		Re	
Flow rate	Water	Blood analogue	Water	Blood analogue
0.43 ml/min	5.89×10^{-6}	1.84×10^{-6}	4	1.33
0.72 ml/min	1.06×10^{-5}	3.31×10^{-6}	7.2	2.4
1.29 ml/min	1.77×10^{-5}	5.52×10^{-6}	12	4
2.57 ml/min	3.53×10^{-5}	1.1×10^{-5}	24	8
3.9 ml/min	5.3×10^{-5}	1.66×10^{-5}	36	12
5 ml/min	6.48×10^{-5}	2.02×10^{-5}	44	14.67

7.3. Fibre channel

In the third experiment it was tested the effect of the non-rigid material, that the real fibres are made from, on the results from the experimental testing. For this purpose velocity profiles in between the fibres from the micro-PIV experiment are compared to velocity profiles from CFD simulation in which the geometry is an exact copy of the experimental channel with fibres, however the fibres are simulated as a rigid body. The experiment is conducted at a constant flow rate of 0.3 ml/min.

The Stokes and Reynolds numbers for the different fluids were evaluated (see table 7.3).

Table 7.3 Stokes and Reynolds numbers for the fibre channel experiment

St		Re	
Water	Blood analogue	Water	Blood analogue
1.69×10^{-5}	5.81×10^{-6}	11.4	3.8

IV. Results

8. Rectangular channel

8.1. Size of interrogation window

Firstly, one image set was processed with two different interrogation windows. On fig. 8.1 A and B are depicted the vectors, evaluated with the 4G Insight software with respectively 64×64 and 64×16 pixels interrogation windows corresponding to 19.2×19.2 and 19.2×4.8 µm spatial resolution. The vector separation in the vertical direction is certainly greater on the left image.

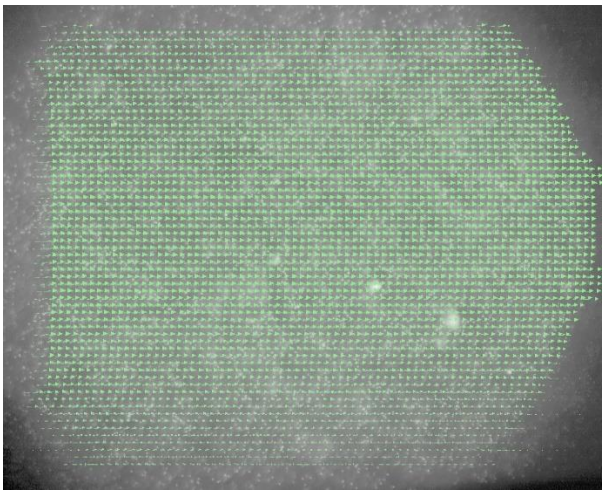

Figure 8.1A Velocity vectors obtained with 64×64 interrogation window.

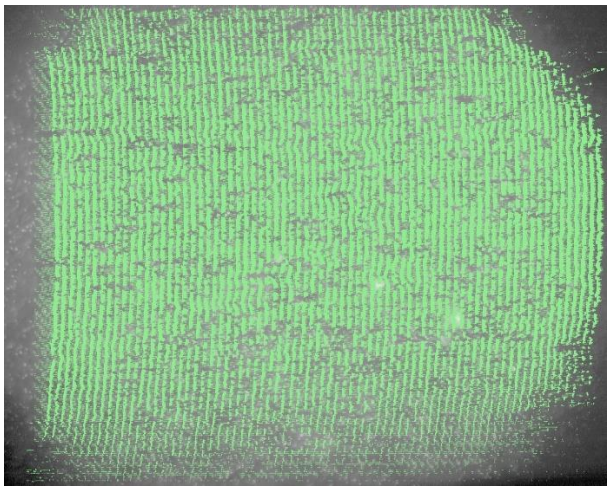

Figure 8.1B Velocity vectors obtained with 64×16 interrogation window.

Figure 8.2 compares the velocity profiles in the plane parallel to the top/bottom plane in the channel obtained with the different interrogation windows with a velocity profile obtained with CFD. The mean absolute percentage error (MAPE) was estimated as 18% for the 64×64 and 11% for the 64×16 interrogation window. It makes impression that the experimental velocities in the vicinity next to the wall (approximately 40 µm away) are very close to zero.

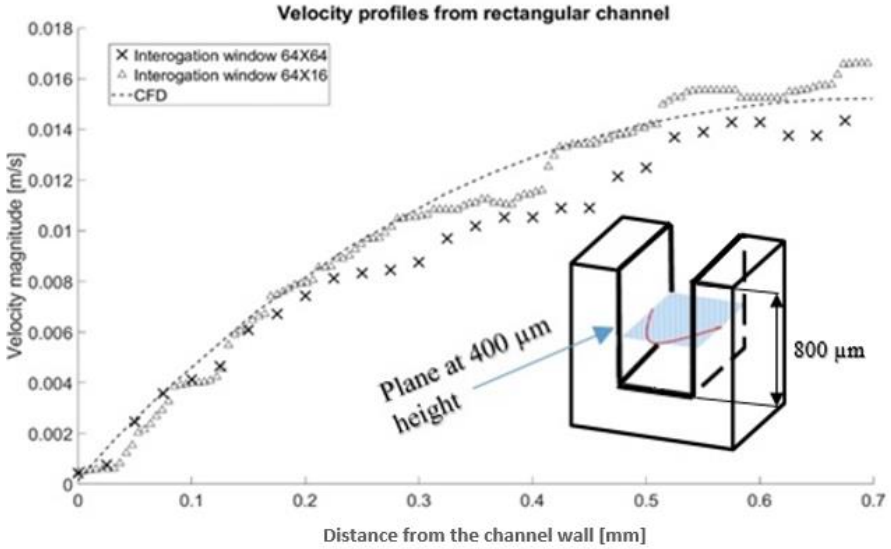

Figure 8.2 Experimental velocity profiles obtained with different interrogation windows compared to CFD velocity profile.

8.2. Working fluids

The velocity profiles (in the same plane as in 8.1) observed in water and in blood analogue are compared to velocity profiles from CFD simulations with the respective viscosity (see fig. 8.3). The MAPE in the case of water is evaluated as 11% and in the case of blood analogue – 9%.

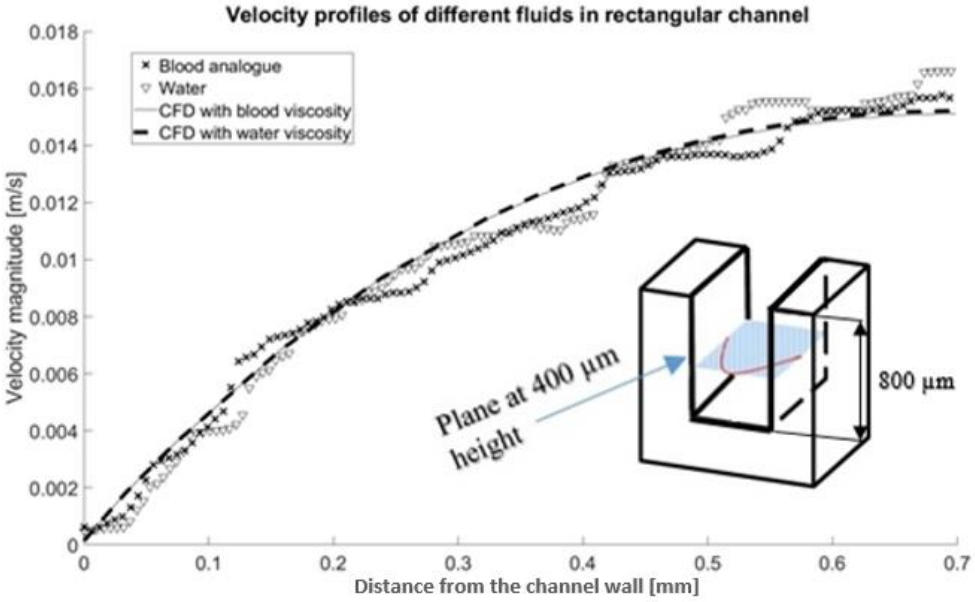

Figure 8.3 Experimental velocity profiles obtained in different working fluids compared to their respective CFD velocity profiles.

8.3. Seeding type

Next, the available seeding particles are compared. On figure 8.4A is displayed an image of the FluoRot particles from the channel at 400 µm height. On figure 8.4B is represented an image of the same place with the Fluoro-Max particles suspended. The image of the particles on the right picture is clearly with much better contrast.

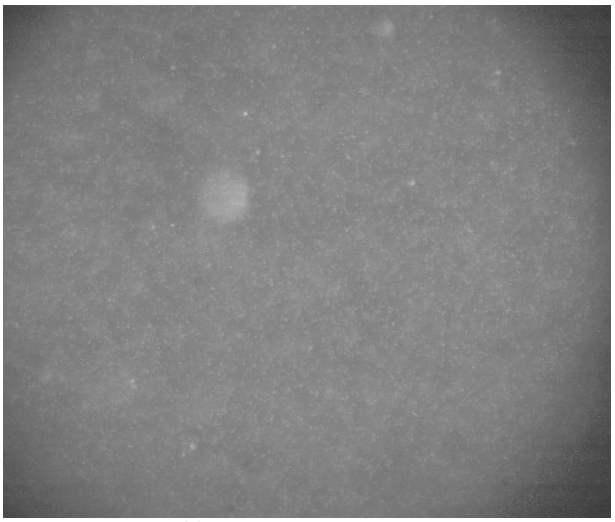

Figure 8.4A Image of fluorescent FluoRot particles.

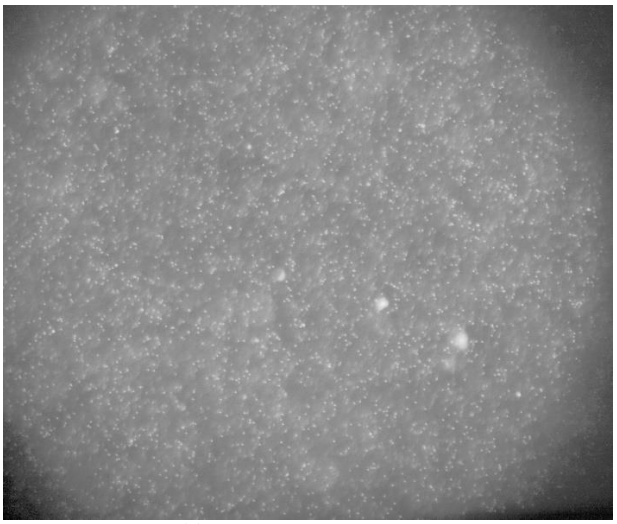

Figure 8.4B Image of fluorescent Fluoro-Max particles.

Comparison of the velocity profiles obtained with the different particles and a velocity profile from a CFD simulation can be observed on figure 8.5. The MAPE was evaluated as 14% by the FluoRot particles and 11% by the Fluoro-Max. It is obvious even for a bare eye, that the profile obtained with the Fluoro-Max particles follows the profile from the simulation much closer. However, the near-zero velocities in the region near the wall are observed again for the both types of particles.

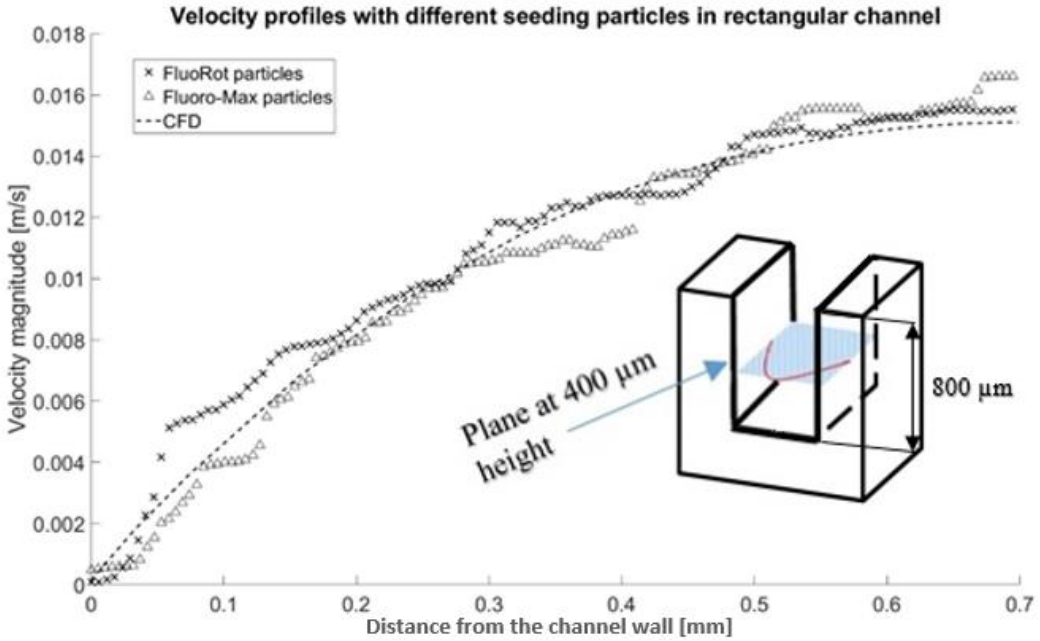

Figure 8.5 Experimental velocity profiles obtained with different seeding particles compared to a CFD velocity profile.

8.4. Seeding concentrations

Images with 10% and 6.66% concentrations of the Fluoro-Max particles are represented respectively on figure 8.6 A and B.

Figure 8.6A Image of fluorescent Fluoro-Max particles – 10 % suspension.

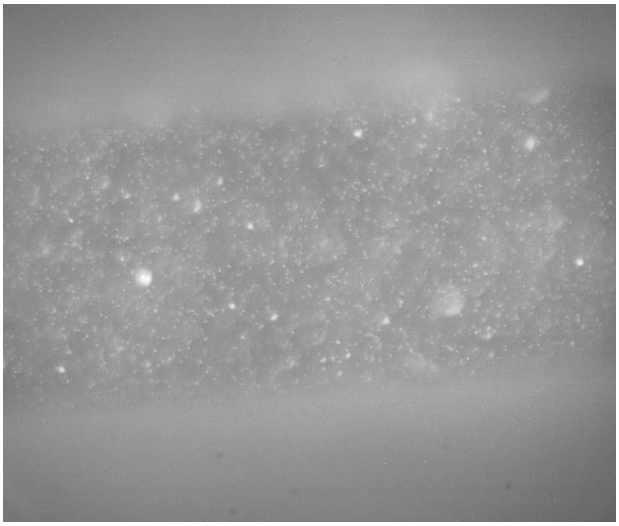

Figure 8.6B Image of fluorescent Fluoro-Max particles – 6.66 % suspension.

8.5. Microscope focus

Lastly, the accuracy of the measurements at different heights of the channel was tested. On figure 8.7 are compared velocity profiles of micro-PIV experiments with a focus on two different heights of the channel – 400 µm and 140 µm, with the velocity profiles at the same places obtained from a CFD simulation. The MAPE for 400 µm height is 14% and 13 % for 140 µm.

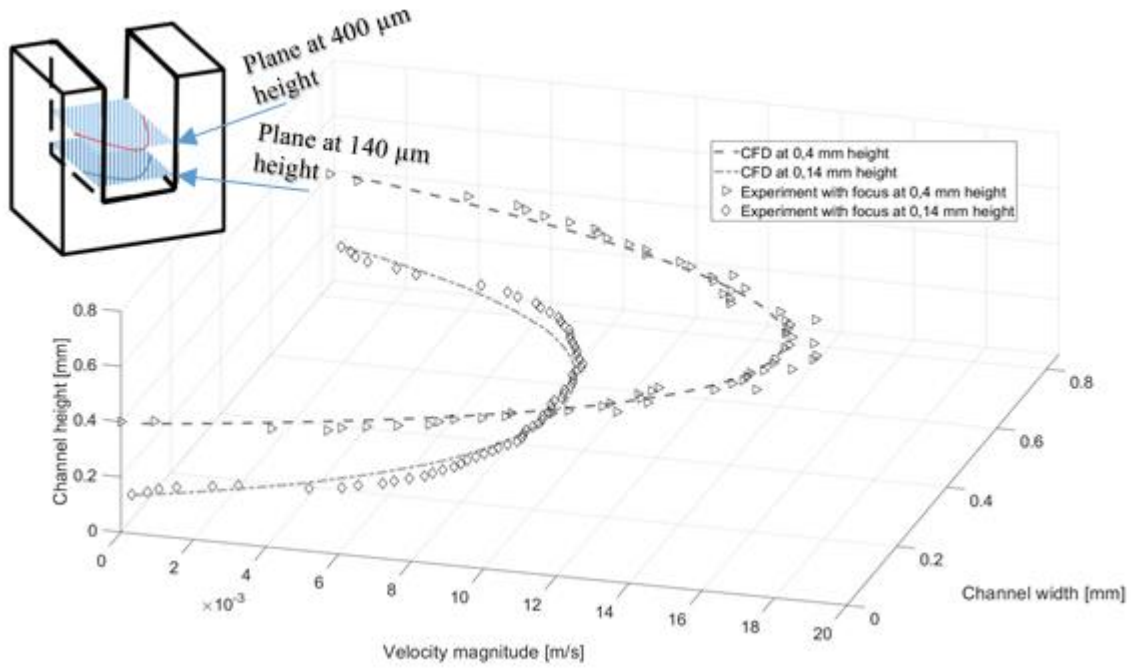

Figure 8.7 Experimental velocity profiles obtained at different heights compared to their respective CFD velocity profiles.

9. Rods channel

9.1. Velocities in water

Figures 9.1 A-H represent contour plots of velocity fields of a transverse flow of water between two rods at height 500 µm. A comparison is made between the results, obtained from CFD simulations (left) and from micro-PIV experiments (right) at flow rates of 1.29, 2.57, 3.9 and 5 ml/min. The simulations match well with the experiment, except at the corners of the image.

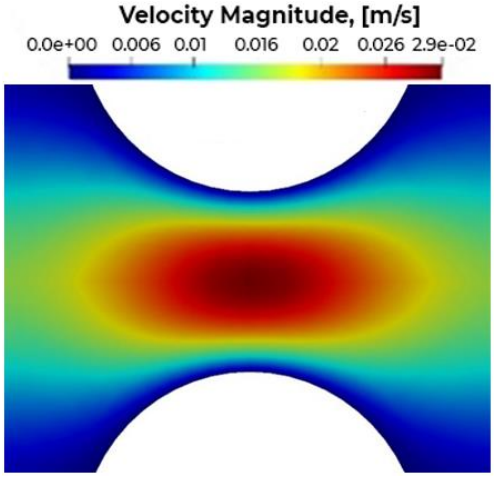

Figure 9.1A Velocity field from CFD simulation with flow rate 1.29 ml/min in the rods channel filled with water.

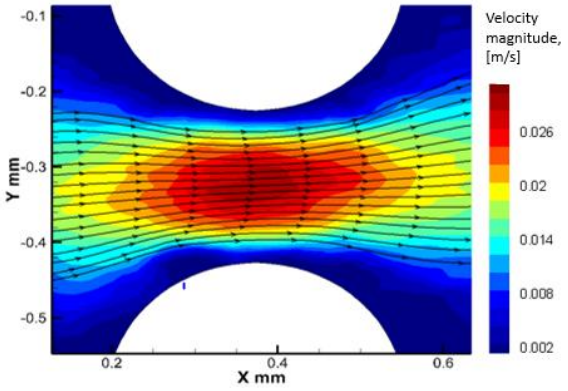

Figure 9.1B Velocity field from micro-PIV experiment with flow rate 1.29 ml/min in the rods channel filled with water.

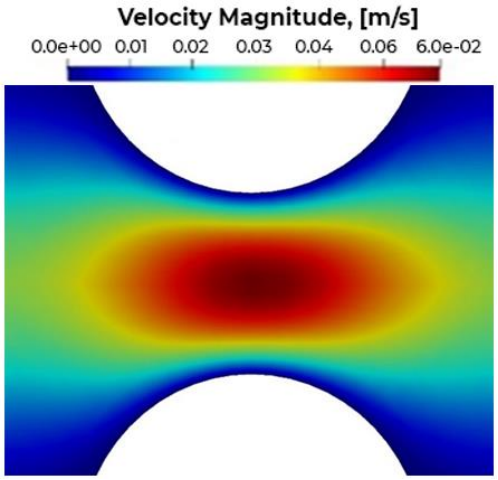

Figure 9.1C Velocity field from CFD simulation with flow rate 2.57 ml/min in the rods channel filled with water.

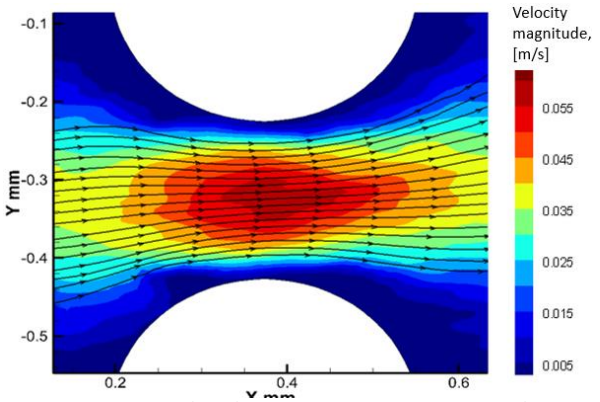

Figure 9.1D Velocity field from micro-PIV experiment with flow rate 2.57 ml/min in the rods channel filled with water.

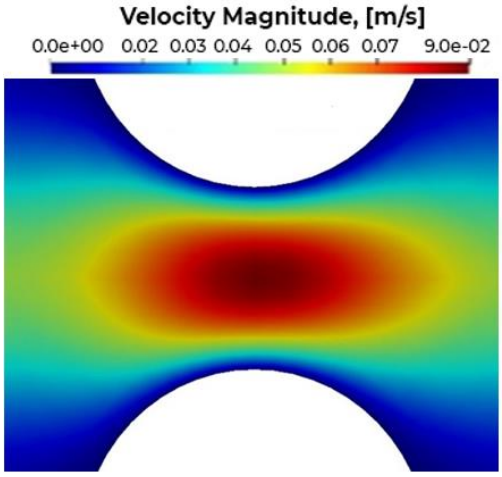

Figure 9.1E Velocity field from CFD simulation with flow rate 3.9 ml/min in the rods channel filled with water.

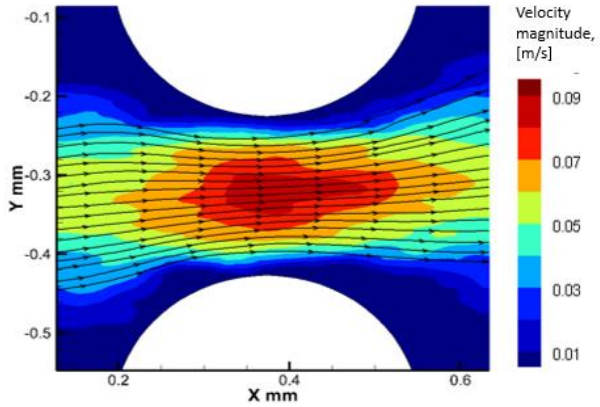

Figure 9.1F Velocity field from micro-PIV experiment with flow rate 3.9 ml/min in the rods channel filled with water.

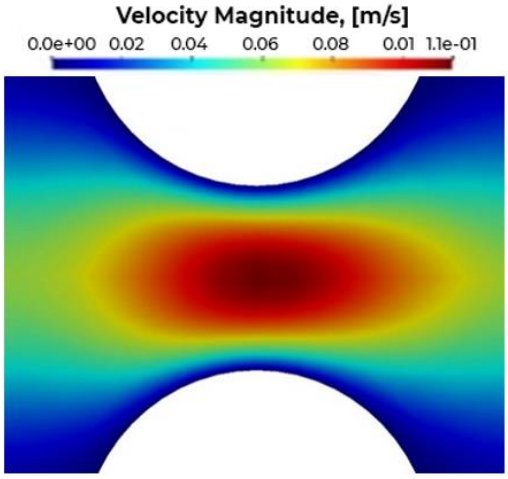

Figure 9.1G Velocity field from CFD simulation with flow rate 5 ml/min in the rods channel filled with water.

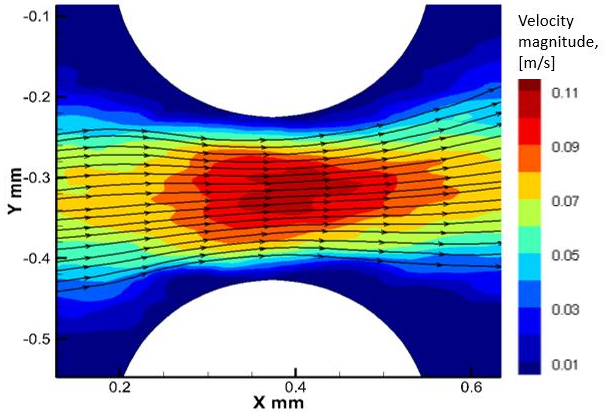

Figure 9.1H Velocity field from micro-PIV experiment with flow rate 5 ml/min in the rods channel filled with water.

Furthermore, the velocity profiles along a line right in the middle of the rods are extracted. The line is defined as the line connecting the centres of the rods and its position (see fig. 9.2) is obtained with an image analysis in MATLAB.

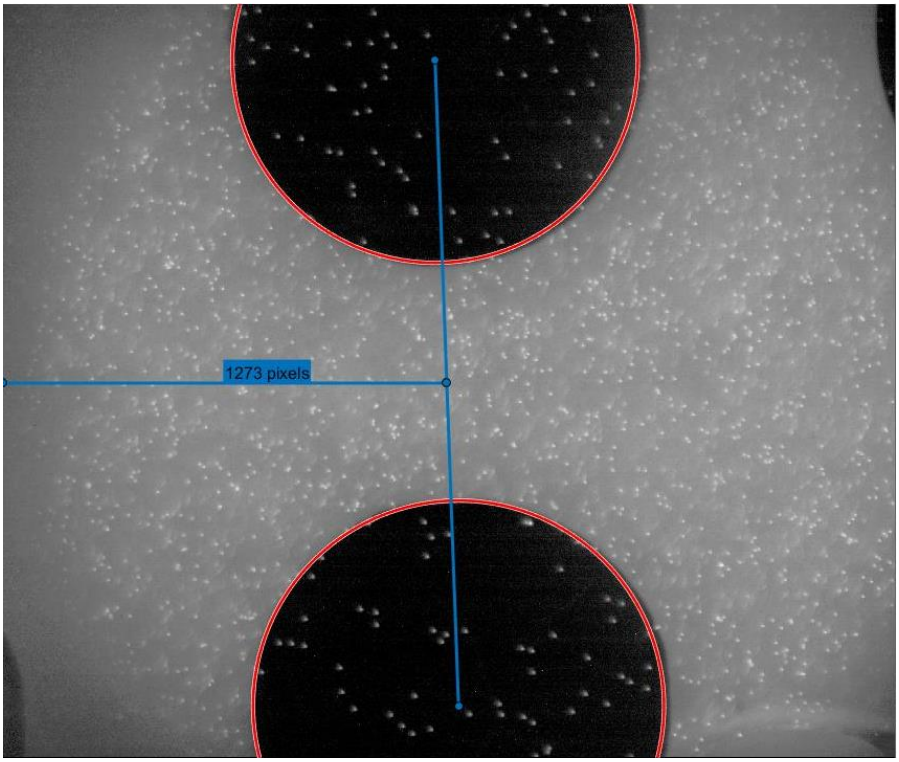

Figure 9.2 Image from the micro-PIV experiment in the rods channel filled with water, analysed with MATLAB function, depicting the position of the line connecting the centres of the rods.

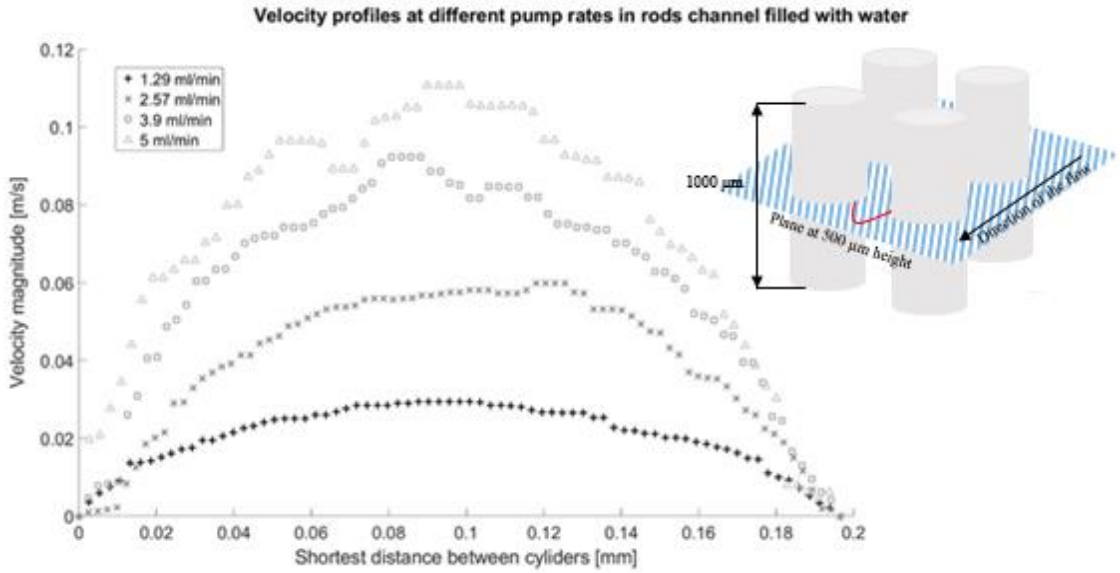

Figure 9.3 Velocity profiles along the line connecting the centres of the rods at different flow rates in the rods channel filled with water.

On figure 9.3 the velocity profiles at different flow rates along the distance between the rods are plotted. It is noticeable that with the increased flow rate the fluctuations in the measured velocity are

increasing as well. Near-zero velocities are also presented in some of the measurements. The MAPE for the different flow rates is estimated in table 9.1:

Table 9.1 MAPE for different flow rates in rods channel filled with water.

Flow rate	1.29 ml/min	2.57 ml/min	3.9 ml/min	5 ml/min
MAPE	13 %	17 %	17 %	12 %

9.2. Velocities with blood analogue

On figure 9.4 A-D can be observed the contour plots of the velocity fields between two rods at 500 µm in the rods channel with a blood analogue as a working fluid. The fields are obtained from micro-PIV experiments at flow rates of 1.29, 2.57, 3.9 and 5 ml/min. The velocities are increasing with the flow rate but also are lower than the ones measured in water.

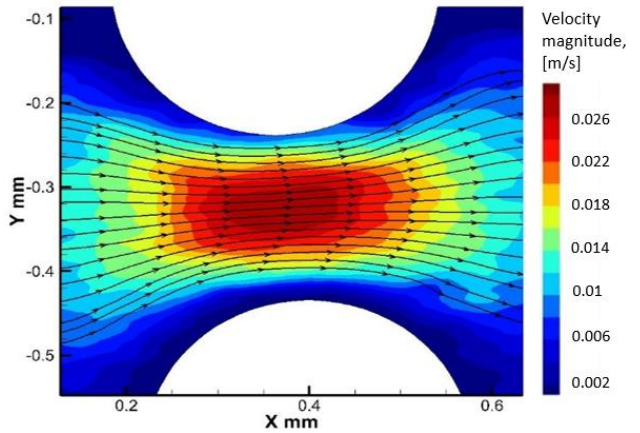

Figure 9.4A Velocity field from micro-PIV experiment with flow rate 1.29 ml/min in the rods channel filled with blood analogue.

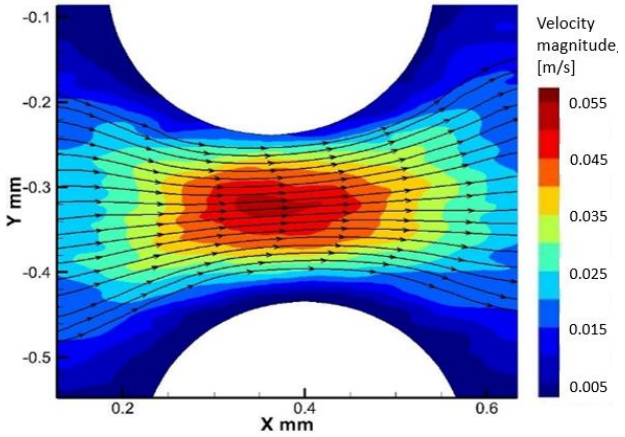

Figure 9.4B Velocity field from micro-PIV experiment with flow rate 2.57 ml/min in the rods channel filled with blood analogue.

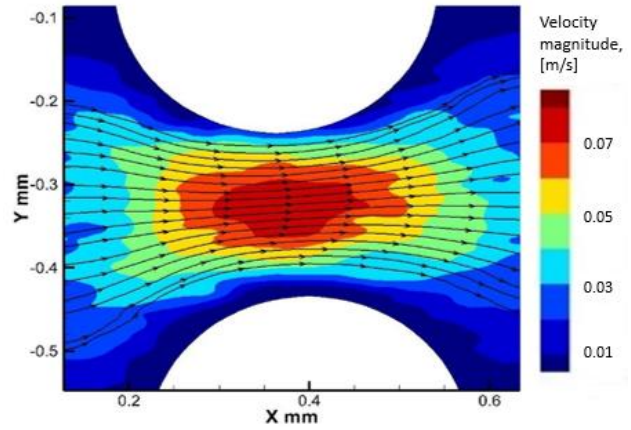

Figure 9.4C Velocity field from micro-PIV experiment with flow rate 3.9 ml/min in the rods channel filled with blood analogue.

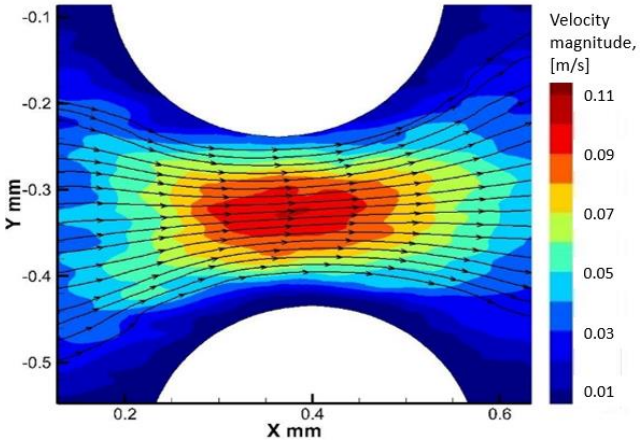

Figure 9.4D Velocity field from micro-PIV experiment with flow rate 5 ml/min in the rods channel filled with blood analogue.

Next, the position of the line connecting the centres of the rods is displayed on figure 9.5 and the velocity profiles along the distance between the rods at the different flow rates are plotted on figure 9.6. The shape of the profiles differs from the profiles obtained in water.

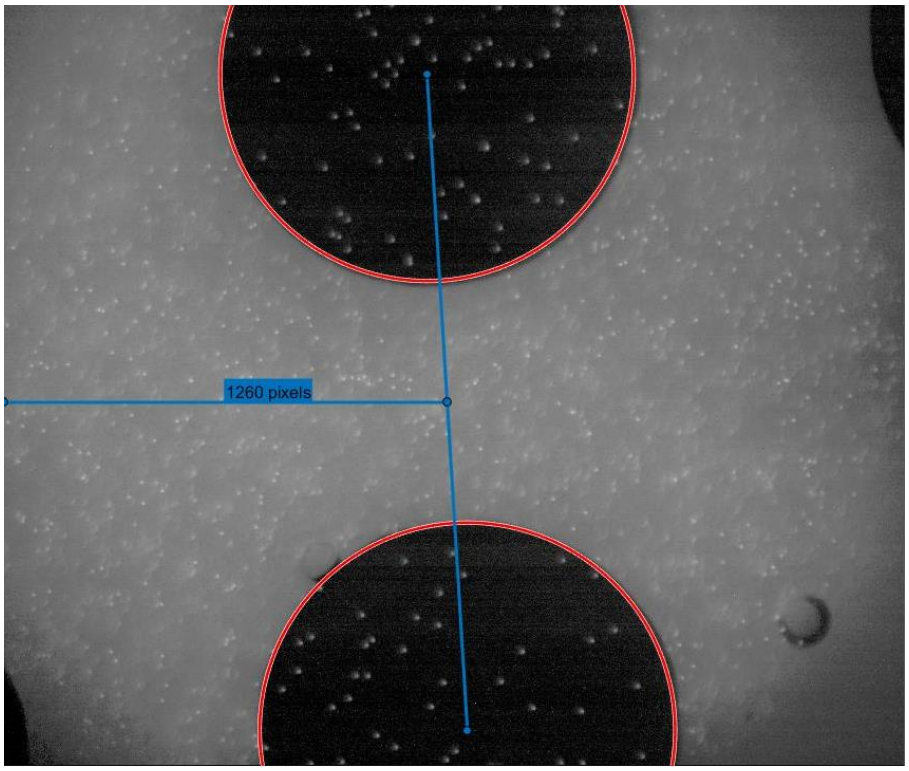

Figure 9.5 Image from the micro-PIV experiment in the rods channel filled with blood analogue, analysed with MATLAB function, depicting the position of the line connecting the centres of the rods.

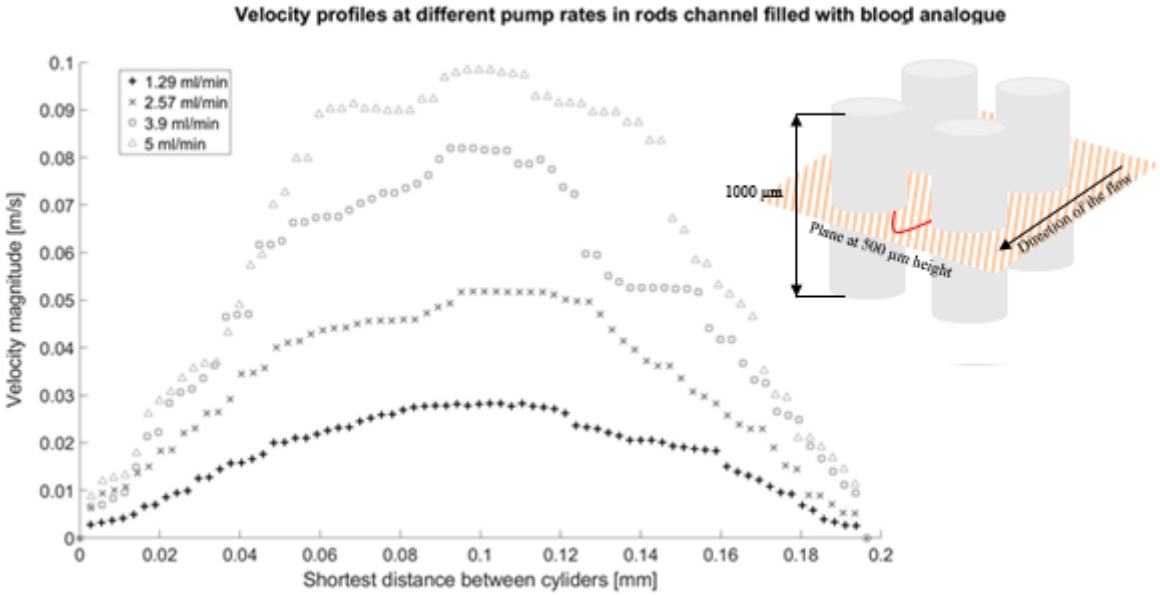

Figure 9.6 Velocity profiles along the line connecting the centres of the rods at different flow rates in the rods channel filled with blood analogue.

9.3. Mass transport and hemolysis

For an estimation of the values of the shear stress and the residence time, needed for the calculation of the hemolysis index, a precise data extraction is done. The values for the strain rate and the velocities along the streamlines are extracted from the region depicted at figure 9.7.

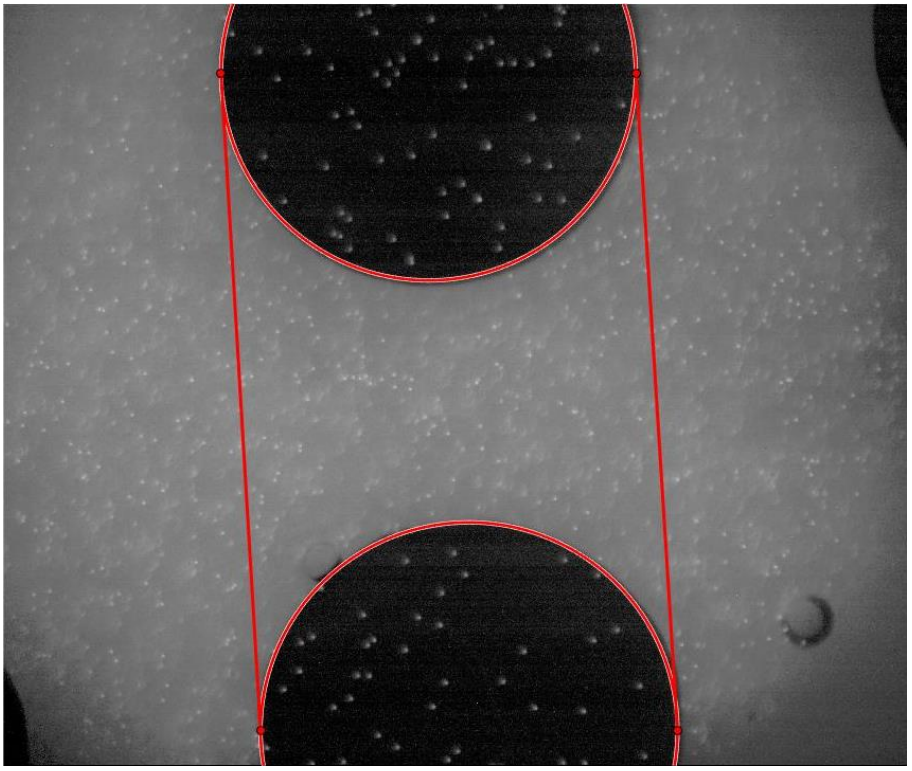

Figure 9.7 Image from the micro-PIV experiment in the rods channel filled with blood analogue, analysed with MATLAB function, depicting the region between the rods from which the data regarding hemolysis estimation is extracted.

On figure 9.8 the hemolysis index, calculated with the Giersiepen-Wurzinger (GW) parameters (see 2.6) and the experimentally derived values for the shear stress at flow rates of 0.43, 0.72, 1.29, 2.57, 3.9 and 5 ml/min, is plotted next to the Sherwood number (Sh). Sh is analytically estimated with the Reynolds numbers (Re) for the respective flow rates (0.43, 0.72, 1.29, 2.57, 3.9 and 5 ml/min), and has the meaning of a mass transport of CO_2 in blood.

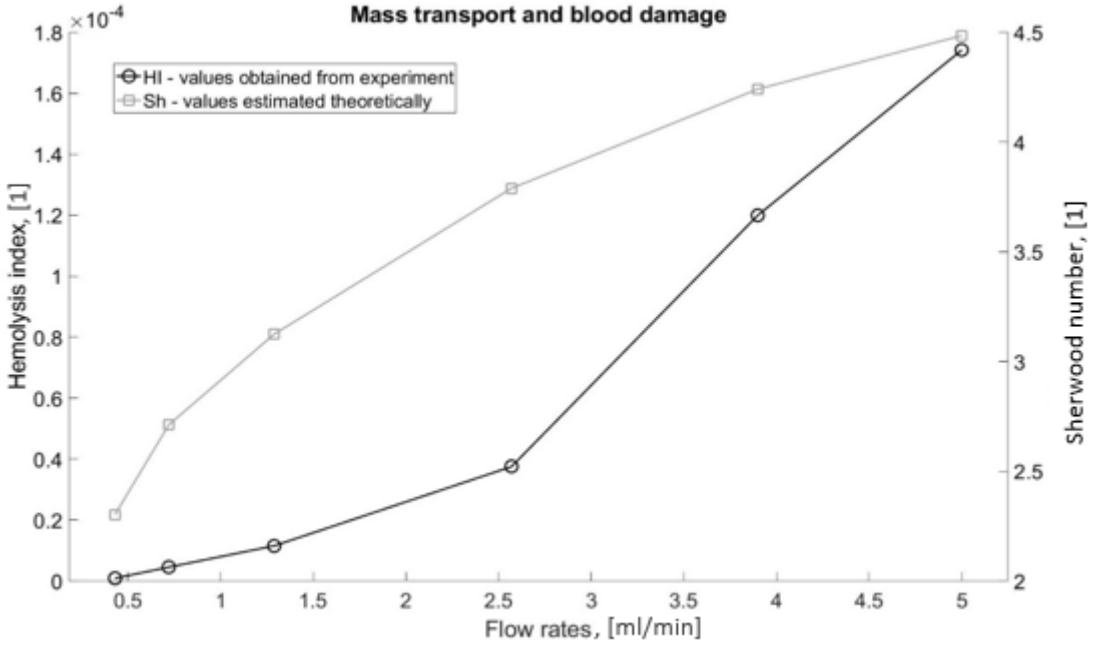

Figure 9.8 Plot of the change of experimentally estimated hemolysis index with the increase of the flow rate and the respective increase of the CO2 mass transport represented by the analytically derived Sherwood number.

10. Fibre channel

The last experiment is an observation of a velocity profile in between the real fibres of a flow parallel to the fibres. The micro-PIV experiment is conducted in a focus plane at 390 µm channel height. Figure 10.1 depicts the velocity profile from the experiment compared to a velocity profile from a CFD simulation. The MAPE for the corresponding vicinity is estimated to be 4%.

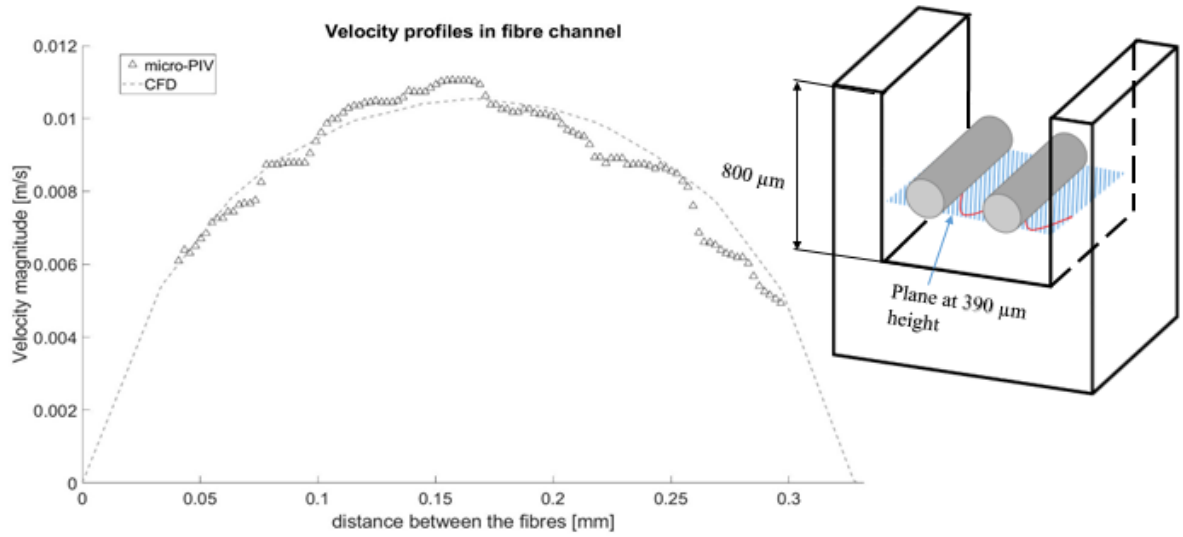

Figure 10.1 Velocity profiles between real PMP fibres from of flow parallel to the fibres. A profile from a micro-PIV experiment is compared to a profile from a CFD simulation.

V. Discussion

11. Rectangular channel

In the first part of this experiment the spatial resolution of the micro-PIV system is tested. It is visible from the images on figure 8.1 A and B that a processing with a smaller interrogation window, corresponding to a higher spatial resolution, results in a field with many more vectors. However, the quality of the vector field obtained with a bigger interrogation window seems to be more homogeneous. This is also the qualification of the 4G Insight software, which classifies 98% of the vectors as "good" in the case of a 64×64 pixels interrogation window and only 76% in the latter case. Anyway, this is only evaluation of the successful use of the cross-correlation function over the region of interest. It has merit in the assumption that a decreased spatial resolution will result in a higher relative number of vectors passing the cross-correlation validation, since in a bigger interrogation window it is more probable to find a distinctive intensity peak, satisfying the SNR as it is represented schematically on figure 11.1.

More reliable way of assessing the measurement accuracy is to estimate the error. With the calculation of MAPE it was established that processing with a higher spatial resolution results in measurements closer to the values from the CFD simulation. Therefore, all the following measurement were processed with an interrogation window 64×16 pixels.

Next, the possibility of using a blood analogue instead of a water in the experimental channel is investigated. The values of the MAPE for both fluids are similar (around 10%), which is a sign that the transparent mixture with viscosity of blood is a reliable source of information regarding the mechanical properties of blood flow, at least in a laminar, Newtonian flow, and it can be further used in experiments including more complex geometries.

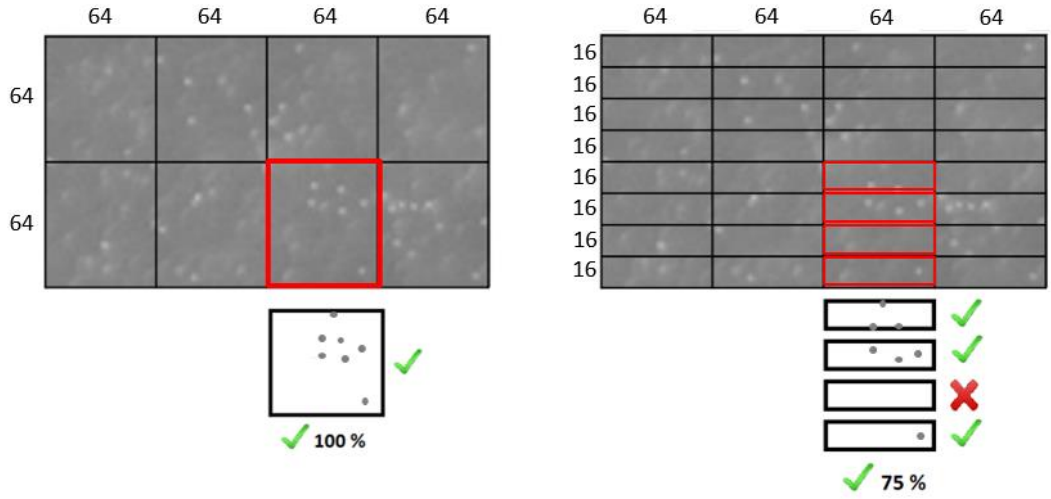

Figure 11.1 Comparison between the pass validation success with 64×64 pixels interrogation window (left) and 64×16 pixels interrogation window (right). From the region outlined in red it is visible that, once the interrogation window is divided in smaller windows, some of newly formed windows lack signal with enough intensity, therefore they cannot produce a valid velocity vector.

By the choice of seeding particles, the MAPE seems to be slightly higher for the FluoRot particles. Moreover, on figure 8.4 it can be observed the images of the fluorescent particles. The Fluoro-Max particles clearly show higher peak intensities with a better image contrast, which would result in more distinctive peaks as an input for the cross-correlation function. This qualitative observation together with the smaller error leads to the choice of the Fluoro-Max particles for the seeding of the next experiments.

The concentration was chosen, at first, to be 10 % particles by volume. However, this resulted in too much light emitted from the particles, presumably from the out-of-focus planes (see fig. 8.6A). Later, the solution was diluted to a 6.66 % concentration, which produced much more acceptable image displayed on figure 8.6B. All further investigations were conducted at the lower concentration. A MAPE estimation was not possible since the processing of the measurement with 10 % concentration did not deliver a sufficient vector field.

As a last part of this experiment it was inspected the possibility and the accuracy of the micro-PIV setup to assess an information, regarding multiple planes of the flow parallel to each other. In this attempt, at similar conditions, a measurement from the central plane of the flow was taken, after which the focus was moved to the plane corresponding to 140 µm height of the channel. The values of the errors for the both cases are similar and sufficiently low. This observation proves the ability of the previously described micro-PIV system to collect the experimental information needed to rebuild 3D velocity profiles.

A general remark, regarding all the velocity profile plots, is that the experimental results at distance very close to the wall (< 50 µm) seem to show much lower velocities than the ones predicted with the CFD. A possible explanation for this is the discrepancy between the refractive index of the cover of the channel and the working fluid. Similar result are declared by Novakova et al. [65]. However, the channel cross-section is rectangular and the refraction boundaries are parallel to each other, hence there is no spatial deformation in the image, which would affect the resulting velocities. Such a deformation would occur by the use of a channel with a circular cross-section. Another reason might be the lower intensity of the light spot away from the image centre and low magnification.

12. Rods channel

By the experiment in a water medium, the velocity fields obtained at different flow rates are compared to velocity fields from CFD simulations. It makes impression on the contour plots on figure 9.1, that there is a good conformity between the simulation and the experiment in the central region of the plot, except for the more pronounced, asymmetric narrowing of the zones with higher velocities in the direction of the flow in the experimental plots. This effect is probably due to the deceleration of the fluid

after passing through the narrow region between the rods. Another contribution to this visual discrepancy might be the post processing of the plots with a linear interpolation and smoothing, together with minor differences in the colour scale. However, the lack of almost any velocity in the corner of the plots, derived from the micro-PIV, is with a high possibility, due to the fact, that the light spot of the laser is circular and is pointed at the centre of the image (see fig. 8.1 A and B, 8.4 A and B, 9.2). Thus, there is not enough intensity of the light in the corners and the motion of the particles cannot be detected.

For a more precise information the velocity profiles at a specific place are compared. The relatively low values of the MAPE for the 4 different velocities present a good agreement between the experiment and the simulation. Moreover, there is no correlation observed between the MAPE values and the increase of the flow rate. As it is visible on figure 9.3, there is a tendency of narrowing the stagnant layer near the walls with the increase of the flow rate. However, the region closest to the wall, which is usually associated with a boundary layer, seems to remain covered in the meaning of velocities close to zero without a change at the different flow rates. This is most probably related to the discrepancy of the refractive indices, discussed above (see 11.). This obstacle is of course very unfortunate, since this part of the profile is of a great interest, due to the information regarding the mass transport hidden there. Another drawback, regarding the comparison of CFD simulations with experiments, is that the velocity data from the simulation is extracted right in the middle of the rods, along a line corresponding to a region with an infinitesimal thickness. In the case of this micro-PIV experiment the velocity data is extracted from a spreadsheet with 74 rows and 265 columns, tilted by 90 degrees. Since the field of view is approximately 710 µm (horizontal axis) times 634 µm (vertical axis), a single row of data contains velocity values for a region with 8.57 µm thickness along the vertical axis of the image (see fig. 12.1 A and B).

Furthermore, by the same experiment conducted with a transparent fluid with the viscosity of blood similar results are observed at different flow rates. The velocity values are slightly lower than these obtained with water, which corresponds to the higher viscosity. The contour plots seem to be more homogeneous and the velocity profiles shape looks more distinctive in the region near to the wall, especially at the slower flow rates. This might be a result of the closer match of the refractive index of the blood analogue (n=1.39) to the one of the channel cover (in the specific case glass – n=1.51), than the refractive index of the water (n=1.33) to the one of the channel cover. Anyway, at the 3.9 and 5 ml/min flow rates the profiles almost completely match each other at a distance up to 40 µm away from the rod, which underlines the uncertainty of the measurements in the regions near the wall.

Next, the values calculated for the hemolysis index in the meaning of a blood damage are compared to the values of the Sherwood number, as estimation of the CO_2 transport between the two fibres and the fluid, for six different flow rates. The very low number for the hemolysis corresponds to the very small area of the region of interest, where the strain rate values are sampled from and the corresponding values for the shear stress are calculated. Another contribution to the low blood damage is the short residence time. As it is mentioned in the theoretical part of this work (see 2.3), the blood is well known for its non-Newtonian behaviour, which leads to the question – is the direct linear conversion of the shear rate (multiplied by the dynamic viscosity) to a shear stress applicable for this case. Since the value for the shear rate for all the experiments with the slowest flow rate (0.43 ml/min) is greater than 750 s^{-1}, we can assume that the behaviour of the blood stays Newtonian for all the other cases (see fig. 2.6 B), therefore the relationship should hold. However, in the first half of the plot, up to 2.57 ml/min, the increase in the two properties of interest is almost similar, whereas from 2.57 to 5 ml/min the hemolysis reaches almost 4.7 times increase and the Sherwood number grows only 1.2 times. In general, the presented values do not predict a very high damage on the blood, but they are responsible only for a very small part of the whole membrane. Perhaps, if these results are integrated over the full length and the respective number of fibres in a membrane oxygenator, it might be considered that the optimal flow velocity in between the fibres is approximately 5-6 mm/s (the velocity corresponding to 2.57 ml/min, displayed on figure 9.6).

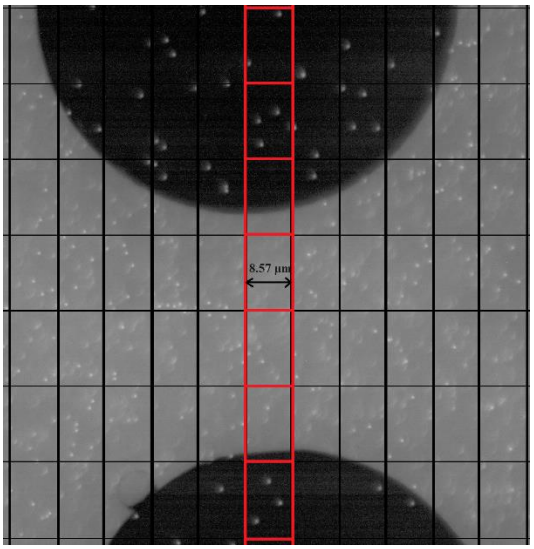

Figure 12.1A Schematic representation of the experimental sampling. Every box from the grid is responsible for one value. The size of the grid is exaggerated for better view.

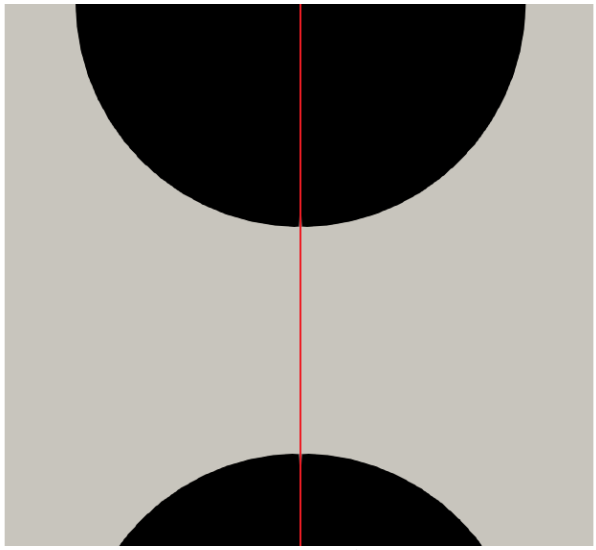

Figure 12.1B Schematic representation of the CFD sampling. The red line is with infinitesimal thickness.

13. Fibre channel

The last experiment comes to prove that, substituting the fibres with acrylic rods with similar dimensions in the previous experiment does not significantly affect the obtained results. On figure 10.1 is represented a comparison of a part of a velocity profile from a micro-PIV experiment, where real PMP fibres are situated parallel to the flow, and a CFD simulation, where the exact fibre location is replicated, but not the elastic properties, thus the fibres are simulated as rigid bodies. Moreover, the reason for comparing only a part of the experimental profile, is that the microscope focus was on the far side of the fibres, therefore the velocities near the fibres are hidden for the light by the fibres their selves and only the middle of the profile is visible (see fig. 13.1). Eventually, the MAPE, occurring by the comparison of the matched parts, is very low (approx. 4%), which would suggest, that the experimental results from the channel with rods, are not essentially influenced by the lack of the elastic properties of the real fibres.

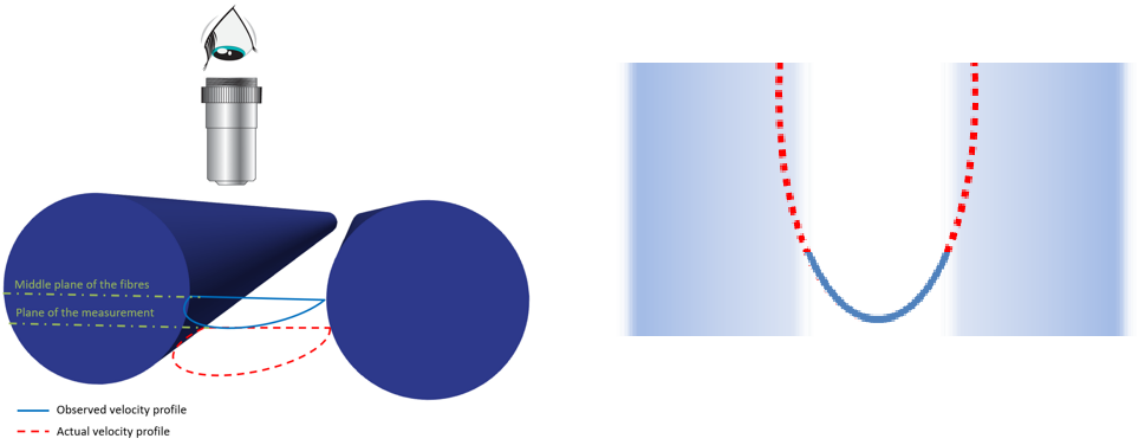

Figure 13.1 Schematic representation of the fibre channel experiment setup in the 3D space (left) and the 2D projection of the plane of view seen from above (right).

14. Accuracy

Generally, the Reynolds and the Stokes numbers for all the experiment were calculated. The values for the Reynolds number do not exceed 44, ensuring laminar flow conditions, and for the Stokes number remain between 10^{-6} and 10^{-5}, guaranteeing that the particles follow firmly the flow.

The depth of correlation of this micro-PIV configuration is estimate as approximately 30 μm. In the centre of the rectangular channel the predicted, with CFD, deviation of the velocity in this range (from -15 to 15 μm in direction normal to the plane of interest) is around 0.2% and in the centre of the rods channel at the fastest flow rate is 0.03%. This low values would suggest that the DOC is small enough to obtain reliable results for the respective plane of interest.

VI. Conclusion

The presented work gives an overview on the use of micro-PIV for validating CFD simulations and testing mechanical properties of blood.

Firstly, important details from the methodology of investigating fluid flow properties with PIV were analysed in a rectangular channel. It was found out that a rectangular interrogation window with a higher resolution in the direction normal to the flow gives more accurate results. Two different types of seeding particles were tested and the better one with diameter of 2 μm was chosen. A concentration of 6.66% particles by volume was found to be optimal for the available micro-PIV configuration. The attempt of using a transparent fluid (mixture of xanthan gum, sucrose and water) with viscosity of blood was also successful. At the end, the ability of deriving velocity profiles from multiple planes, for the purpose of 3D velocity profile reconstruction, was successfully tested. The obtained velocity profiles from the experiments were also analysed to what extend do they deviate from CFD simulations with the same conditions. The MAPE evaluated for all the cases was between 9 and 18 %. However, the main issue of the experimental results remain the mismatch of the refractive indices between the working fluid and the channel cover.

Next, a channel that resembles the cross-section of an ECMO-module was built in order to observe a transverse flow through fibres. The flow was tested with 4 different flow rates corresponding to velocities of 3, 6, 9 and 11 mm/s in between the fibres. CFD simulation representing the same channel were created and the results were compared to the experiments. The mean error for the different velocities was between 12 and 17%. Furthermore, the hemolysis between two fibres was estimated from the experimental results and was compared to the analytically evaluated Sherwood number for the respective velocities. An optimal value of 6 mm/s was proposed for the velocity between the fibres. This experiment suffers the same drawback as the previous one – the mismatched refractive indices. Another important part for improvement is the validation of hemolysis estimation with an explicit experiment with real blood.

At last, it was verified the use of rigid rods in the second experiment instead of real PMP fibres. A channel with two real fibres, fixed parallel to the flow, was investigated with micro-PIV and the results were compared to a CFD simulation, where the elastic properties were not considered. The mean deviation between the experiment and the simulation was as low as 4 %.

Future work

To improve the general methodology, it will be important to, firstly, make measurements in the rectangular channel with a microscope objective with higher magnification and respectively with higher spatial resolution near the walls. The results can be compared to these from this thesis and the deviation can be evaluated.

Furthermore, velocity profiles from multiple planes can be sampled from the rods channel and a 3D profile of the velocity between the rods can be rebuilt.

It would be of a great interest to validate the hemolysis estimation from the micro-PIV results with explicit hemolysis tests. This would mean to make an in vitro test with blood looped through the rods channel and to measure the haemoglobin release in the plasma.

List of abbreviations

$\vec{F}_c$	Vector of convective fluxes
$\vec{F}_v$	Vector of viscous fluxes
$\hat{y}_i$	Predicted value
D_{AB}	Diffusion coefficient
D_{Sp}	Diffraction limited spot size
D_a	Aperture diameter
D_{effCO_2}	Effective diffusion coefficient of CO_2
II_τ	Second invariant of the viscous stress tensor
$\overline{M}$	Mass matrix
$\vec{Q}$	Volume sources
$\vec{R}$	Residual
R_I	Auto-correlation function
R_{II}	Cross-correlation function
$\overrightarrow{W}$	Vector of conservative variables
d_p	Particle diameter
d_s	Airy disc diameter
$f^\#$	f-number
k_c	Mass transport coefficient
l_f	flow characteristic length
s_i	Distance between objective lens
u_f	Fluid flow velocity
y_i	Experimental value
$\dot{\varepsilon}$	Strain rate
ρ_p	Density of the particle
$\overline{\tau}$	Shear stress
τ_s	Characteristic time
µs	Micro-second
2D	Two-dimensional
3D	There-dimensional
ADP	Adenosine diphosphate
CCD	Charge coupled device
CFD	Computational fluid dynamics
CMOS	Complementary metal-oxide-semiconductor
CNC	Computer numerical control
CO_2	Carbon dioxide
DOC, z_{corr}	Depth of correlation
ECMO	Extracorporeal membrane oxygenation
FEP	Fluorinated ethylene propylene
GW	Giersiepen-Wurzinger
H	Hemolysis
Hb	Haemoglobin

HFO	Hollow fibre oxygenator
HO	Heuser-Opitz
Hz	Herz
kg	Kilogram
LVAD	Left ventricular assist devices
m^3	Cubic meter
MAPE	Mean absolute percentage error
mJ	Millijoule
ml/min	Milliliter per minute
Mm	Millimeter
MOS-FET	Metal-oxide semiconductor field-effective transistors
Ms	Millisecond
Nd	Neodym
nm	Nano-meter
O_2	Oxygen
Pa	Pascal
PIV	Particle Image Velocimetry
PMP	Polymethylpentene
ppm	Parts per million
Ps	Picosecond
PTV	Particle tracking velocimetry
RBC	Red blood cell
s	Second
SHG	Second harmonic generator
SNR	Signal-to-noise ratio
VAD	Ventricular assist devices
WBC	White blood cell
YAG	Yttrium-aluminum-garnet
ZT	Zhang
δ	Film layer thickness
τ	Viscous stress tensor
Ω	Control volume
H	Enthalpy
L	Characteristic length
M	Magnification factor
NA	Numerical aperture
Re	Reynolds number
Sh	Sherwood number
Sc	Schmidt number
St	Stokes number
f	Focal length
t	Time, exposure time, residence time
tr	Trace of tensor
u	Velocity
ε	Porosity of PMP fibres
λ	Wavelength
μ	Dynamic viscosity
μm	Micro-meter
ν	Kinematic viscosity

List of figures

List of tables

References

[1] J. Novotný and L. Manoch, 'THE CRITERION OF CHOOSING THE PROPER SEEDING PARTICLES', *Eng. Mech.*, p. 10, 2012.
[2] M. Schmidt, G. Tachon, C. Devilliers, G. Muller, G. Hekimian, N. Bréchot, S. Merceron, C.E. Luyt, J.L. Trouillet, J. Chastre, P. Leprince, A. Combes. Blood oxygenation and decarboxylation determinants during venovenous ECMO for respiratory failure in adults. Intensive Care Med 39, 838–846 (2013). https://doi.org/10.1007/s00134-012-2785-8
[3] X. Song, A. L. Throckmorton, H. G. Wood, J. F. Antaki, and D. B. Olsen, 'Computational Fluid Dynamics Prediction of Blood Damage in a Centrifugal Pump', *Artif. Organs*, vol. 27, no. 10, pp. 938–941, 2003, doi: 10.1046/j.1525-1594.2003.00026.x.
[4] H. Yu, S. Engel, G. Janiga, and D. Thévenin, 'A Review of Hemolysis Prediction Models for Computational Fluid Dynamics', *Artif. Organs*, vol. 41, no. 7, pp. 603–621, Jul. 2017, doi: 10.1111/aor.12871.
[5] M. Giersiepen, L. J. Wurzinger, R. Opitz, and H. Reul, 'Estimation of Shear Stress-related Blood Damage in Heart Valve Prostheses - in Vitro Comparison of 25 Aortic Valves', *Int. J. Artif. Organs*, vol. 13, no. 5, pp. 300–306, May 1990, doi: 10.1177/039139889001300507.
[6] R. J. Adrian, 'Twenty years of particle image velocimetry', *Exp. Fluids*, vol. 39, no. 2, pp. 159–169, Aug. 2005, doi: 10.1007/s00348-005-0991-7.
[7] M. Raffel, C. E. Willert, F. Scarano, C. J. Kähler, S. T. Wereley, and J. Kompenhans, *Particle Image Velocimetry: A Practical Guide*. Springer, 2018.
[8] C. G. Caro, T. J. Pedley, R. C. Schroter, and W. A. Seed, *The Mechanics of the Circulation*. Cambridge University Press, 2012.
[9] G. J. Tortora and B. Derrickson, *Principles of anatomy & physiology*, 13th ed. Hoboken, NJ: Wiley, 2012.
[10] Y. C. Fung, *Biomechanics: Mechanical Properties of Living Tissues*. Springer Science & Business Media, 2013.
[11] L. Waite, *Biofluid Mechanics in Cardiovascular Systems*. McGraw Hill Professional, 2005.

[12] J. R. Levick, *An Introduction to Cardiovascular Physiology*. Butterworth-Heinemann, 2013.
[13] R. Fåhræus and T. Lindqvist, 'The viscosity of the blood in narrow capillary tubes', *Am. J. Physiol.-Leg. Content*, vol. 96, no. 3, pp. 562–568, Mar. 1931, doi: 10.1152/ajplegacy.1931.96.3.562.
[14] H. Ye, Z. Shen, and Y. Li, 'Interplay of deformability and adhesion on localization of elastic micro-particles in blood flow', *J. Fluid Mech.*, vol. 861, pp. 55–87, Feb. 2019, doi: 10.1017/jfm.2018.890.
[15] 'The TeachMeSeries - Educational Healthcare Resources'. [Online]. Available: http://teachmeseries.com/. [Accessed: 30-Oct-2019].
[16] B. Swynghedauw, 'Molecular Mechanisms of Myocardial Remodeling', *Physiol. Rev.*, vol. 79, no. 1, pp. 215–262, Jan. 1999, doi: 10.1152/physrev.1999.79.1.215.
[17] M. A. Pfeffer and E. Braunwald, 'Ventricular remodeling after myocardial infarction. Experimental observations and clinical implications', *Circulation*, vol. 81, no. 4, pp. 1161–1172, Apr. 1990, doi: 10.1161/01.cir.81.4.1161.
[18] E.J. Birks, P.D. Tansley, J. Hardy, R.S. George, C.T. Bowles, M. Burke, N.R. Banner, A., Yacoub M.H. Khaghani, 'Left Ventricular Assist Device and Drug Therapy for the Reversal of Heart Failure', *N. Engl. J. Med.*, vol. 355, no. 18, pp. 1873–1884, Nov. 2006, doi: 10.1056/NEJMoa053063.
[19] C. Reider, J. Moon, V. Ramesh, R. Montes, J. Campos, B. Herold, P. Martinez-Legazpi, L. Rossini, J. C. del Alamo, W. Dembitsky, K. May-Newman. 'Intraventricular thrombus formation in the LVAD-assisted heart studied in a mock circulatory loop', *Meccanica*, vol. 52, no. 3, pp. 515–528, Feb. 2017, doi: 10.1007/s11012-016-0433-z.
[20] M. S. Slaughter, J. G. Rogers, C. A. Milano, S. D. Russell, J. V. Conte, D. Feldman, B. Sun, A. J. Tatooles, R. M. Delgado, J. W. Long, T. C. Wozniak, W. Ghumman, D. J. Farrar, O. H. Frazier, 'Advanced Heart Failure Treated with Continuous-Flow Left Ventricular Assist Device', *N. Engl. J. Med.*, vol. 361, no. 23, pp. 2241–2251, Dec. 2009, doi: 10.1056/NEJMoa0909938.
[21] Y. Sugii, R. Okuda, K. Okamoto, and H. Madarame, 'Velocity measurement of both red blood cells and plasma of *in vitro* blood flow using high-speed micro PIV technique', *Meas. Sci. Technol.*, vol. 16, no. 5, pp. 1126–1130, May 2005, doi: 10.1088/0957-0233/16/5/011.
[22] H. L. Goldsmith and J. C. Marlow, 'Flow behavior of erythrocytes. II. Particle motions in concentrated suspensions of ghost cells', *J. Colloid Interface Sci.*, vol. 71, no. 2, pp. 383–407, Sep. 1979, doi: 10.1016/0021-9797(79)90248-0.
[23] H. L. Goldsmith and V. T. Turitto, 'Rheological aspects of thrombosis and haemostasis: basic principles and applications. ICTH-Report--Subcommittee on Rheology of the International Committee on Thrombosis and Haemostasis', *Thromb. Haemost.*, vol. 55, no. 3, pp. 415–435, Jun. 1986.
[24] R. Lima, S. Wada, K. Tsubota, and T. Yamaguchi, 'Confocal micro-PIV measurements of three-dimensional profiles of cell suspension flow in a square microchannel', *Meas. Sci. Technol.*, vol. 17, no. 4, pp. 797–808, Mar. 2006, doi: 10.1088/0957-0233/17/4/026.
[25] R. Lima, 'Analysis of the blood flow behavior through microchannels by a confocal micro-PIV/PTV system', 2007.
[26] 'Artificial Organ Engineering - Maria Cristina Annesini, Luigi Marrelli, Vincenzo Piemonte, Luca Turchetti - Google Books'. [Online]. Available: https://books.google.at/books/about/Artificial_Organ_Engineering.html?id=A22zDAAAQBAJ&printsec=frontcover&source=kp_read_button&redir_esc=y#v=onepage&q&f=false. [Accessed: 04-Nov-2019].
[27] S. F. Marasco, G. Lukas, M. McDonald, J. McMillan, and B. Ihle, 'Review of ECMO (Extra Corporeal Membrane Oxygenation) Support in Critically Ill Adult Patients', *Heart Lung Circ.*, vol. 17, pp. S41–S47, Jan. 2008, doi: 10.1016/j.hlc.2008.08.009.
[28] S. Allen, D. Holena, M. McCunn, B. Kohl, and B. Sarani, 'A Review of the Fundamental Principles and Evidence Base in the Use of Extracorporeal Membrane Oxygenation (ECMO) in Critically Ill Adult Patients', *J. Intensive Care Med.*, vol. 26, no. 1, pp. 13–26, Jan. 2011, doi: 10.1177/0885066610384061.
[29] S. J. Finney, 'Extracorporeal support for patients with acute respiratory distress syndrome', *Eur. Respir. Rev.*, vol. 23, no. 133, pp. 379–389, Sep. 2014, doi: 10.1183/09059180.00005514.

[30] R. M. Arensman, B. L. Short, and D. Stephens, '40 - Extracorporeal Membrane Oxygenation', in *Assisted Ventilation of the Neonate (Sixth Edition)*, J. P. Goldsmith, E. H. Karotkin, M. Keszler, and G. K. Suresh, Eds. Elsevier, 2017, pp. 434-445.e1.
[31] L.-S. Wan, Z.-M. Liu, and Z.-K. Xu, 'Surface engineering of macroporous polypropylene membranes', *Soft Matter*, vol. 5, no. 9, p. 1775, 2009, doi: 10.1039/b813600a.
[32] U. F. O. Themes, 'Extracorporeal Membrane Oxygenation in Infants and Children', *Thoracic Key*, 07-Jun-2016. [Online]. Available: https://thoracickey.com/extracorporeal-membrane-oxygenation-in-infants-and-children/. [Accessed: 05-Nov-2019].
[33] C. Bludszuweit, 'Model for a General Mechanical Blood Damage Prediction', *Artif. Organs*, vol. 19, no. 7, pp. 583–589, 1995, doi: 10.1111/j.1525-1594.1995.tb02385.x.
[34] C. Bludszuweit, 'Three-Dimensional Numerical Prediction of Stress Loading of Blood Particles in a Centrifugal Pump', *Artif. Organs*, vol. 19, no. 7, pp. 590–596, 1995, doi: 10.1111/j.1525-1594.1995.tb02386.x.
[35] B. Thamsen, B. Blümel, J. Schaller, C. O. Paschereit, K. Affeld, L. Goubergrits, U. Kertzscher, 'Numerical Analysis of Blood Damage Potential of the HeartMate II and HeartWare HVAD Rotary Blood Pumps', *Artif. Organs*, vol. 39, no. 8, pp. 651–659, 2015, doi: 10.1111/aor.12542.
[36] L. J. Wurzinger, R. Opitz, P. Blasberg, and H. Schmid-Schönbein, 'Platelet and Coagulation Parameters Following Millisecond Exposure to Laminar Shear Stress', *Thromb. Haemost.*, vol. 53, no. 2, pp. 381–386, Apr. 1985, doi: 10.1055/s-0038-1657744.
[37] D. Arora, 'Computational hemodynamics: Hemolysis and viscoelasticity', Thesis, 2006.
[38] D. Arora, M. Behr, and M. Pasquali, 'Hemolysis Estimation in a Centrifugal Blood Pump Using a Tensor-based Measure', *Artif. Organs*, vol. 30, no. 7, pp. 539–547, 2006, doi: 10.1111/j.1525-1594.2006.00256.x.
[39] D. D. Wachter and P. Verdonck, 'Numerical Calculation of Hemolysis Levels in Peripheral Hemodialysis Cannulas', *Artif. Organs*, vol. 26, no. 7, pp. 576–582, 2002, doi: 10.1046/j.1525-1594.2002.07079.x.
[40] G. Heuser and R. Opitz, 'A Couette viscometer for short time shearing of blood', *Biorheology*, vol. 17, no. 1–2, pp. 17–24, Jan. 1980, doi: 10.3233/BIR-1980-171-205.
[41] T. Zhang, M. E. Taskin, H. Fang, A. Pampori, R. K. Jarvik, B. P. Griffith, Z. J. Wu, 'Study of Flow-Induced Hemolysis Using Novel Couette-Type Blood-Shearing Devices', *Artif. Organs*, vol. 35, no. 12, pp. 1180–1186, 2011, doi: 10.1111/j.1525-1594.2011.01243.x.
[42] G. V. Merrett, C. D. Metcalf, D. Zheng, S. Cunningham, S. Barrow, and S. H. Demain, 'Design and qualitative evaluation of tactile devices for stroke rehabilitation', in *IET Seminar on Assisted Living 2011*, 2011, pp. 1–6, doi: 10.1049/ic.2011.0025.
[43] Y. Sugii, S. Nishio, and K. Okamoto, '*In vivo* PIV measurement of red blood cell velocity field in microvessels considering mesentery motion', *Physiol. Meas.*, vol. 23, no. 2, pp. 403–416, May 2002, doi: 10.1088/0967-3334/23/2/315.
[44] N. Pedersen, P. S. Larsen, and C. B. Jacobsen, 'Flow in a Centrifugal Pump Impeller at Design and Off-Design Conditions—Part I: Particle Image Velocimetry (PIV) and Laser Doppler Velocimetry (LDV) Measurements', *J. Fluids Eng.*, vol. 125, no. 1, pp. 61–72, Jan. 2003, doi: 10.1115/1.1524585.
[45] X. Yang, X. Gui, H. Huang, Y. Shen, Z. Yu, and Y. Zhang, 'Particle image velocimetry experimental and computational investigation of a blood pump', *J. Therm. Sci.*, vol. 21, no. 3, pp. 262–268, Jun. 2012, doi: 10.1007/s11630-012-0543-4.
[46] R. B. Medvitz, V. Reddy, S. Deutsch, K. B. Manning, and E. G. Paterson, 'Validation of a CFD Methodology for Positive Displacement LVAD Analysis Using PIV Data', *J. Biomech. Eng.*, vol. 131, no. 11, pp. 111009-111009–9, Oct. 2009, doi: 10.1115/1.4000116.
[47] B. Su, L. P. Chua, and X. Wang, 'Validation of an Axial Flow Blood Pump: Computational Fluid Dynamics Results Using Particle Image Velocimetry', *Artif. Organs*, vol. 36, no. 4, pp. 359–367, 2012, doi: 10.1111/j.1525-1594.2011.01362.x.
[48] L. PRANDTL, 'Ueber flussigkeitsbewegung bei sehr kleiner reibung', *Verhandl III Intern. Math-Kong Heidelb. Teubner Leipz. 1904*, pp. 484–491, 1904.
[49] J. C. Rotta, *Die Aerodynamische Versuchsanstalt in Göttingen, ein Werk Ludwig Prandtls: ihre Geschichte von den Anfängen bis 1925*. Göttingen: Vandenhoeck & Ruprecht, 1990.
[50] C. Tropea, A. L. Yarin, and J. F. Foss, Eds., *Springer handbook of experimental fluid mechanics*. Berlin: Springer, 2007.

[51] C. D. Meinhart, S. T. Wereley, and M. H. B. Gray, ‘Volume illumination for two-dimensional particle image velocimetry’, *Meas. Sci. Technol.*, vol. 11, no. 6, pp. 809–814, May 2000, doi: 10.1088/0957-0233/11/6/326.
[52] S. T. Wereley and C. D. Meinhart, ‘Micron-Resolution Particle Image Velocimetry’, in *Microscale Diagnostic Techniques*, K. S. Breuer, Ed. Berlin, Heidelberg: Springer, 2005, pp. 51–112.
[53] C. D. Meinhart and S. T. Wereley, ‘The theory of diffraction-limited resolution in microparticle image velocimetry’, *Meas. Sci. Technol.*, vol. 14, no. 7, pp. 1047–1053, Jun. 2003, doi: 10.1088/0957-0233/14/7/320.
[54] E. Hecht, *Optics*. Reading, Mass.: Addison-Wesley, 2002.
[55] J. W. Goodman, *Introduction to Fourier Optics*. Roberts and Company Publishers, 2005.
[56] R. J. Adrian and C.-S. Yao, ‘Pulsed laser technique application to liquid and gaseous flows and the scattering power of seed materials’, *Appl. Opt.*, vol. 24, no. 1, pp. 44–52, Jan. 1985, doi: 10.1364/AO.24.000044.
[57] M. G. Olsen and R. J. Adrian, ‘Out-of-focus effects on particle image visibility and correlation in microscopic particle image velocimetry’, *Exp. Fluids*, vol. 29, no. 1, pp. S166–S174, Dec. 2000, doi: 10.1007/s003480070018.
[58] C. E. N. V. and C. E. Ltd 2002-2017, ‘CCD and CMOS sensors’, *Canon Professional Network*. [Online]. Available: https://cpn.canon-europe.com/content/education/infobank/capturing_the_image/ccd_and_cmos_sensors.do. [Accessed: 14-Nov-2019].
[59] J. Westerweel, ‘Fundamentals of digital particle image velocimetry’, *Meas. Sci. Technol.*, vol. 8, no. 12, pp. 1379–1392, Dec. 1997, doi: 10.1088/0957-0233/8/12/002.
[60] J. Westerweel, ‘Efficient detection of spurious vectors in particle image velocimetry data’, *Exp. Fluids*, vol. 16, no. 3, pp. 236–247, Feb. 1994, doi: 10.1007/BF00206543.
[61] ‘Computational fluid dynamics’, *Wikipedia*. 13-Nov-2019.
[62] J. Blazek, *Computational Fluid Dynamics: Principles and Applications*. Butterworth-Heinemann, 2015.
[63] L. Campo-Deaño, R. P. A. Dullens, D. G. A. L. Aarts, F. T. Pinho, and M. S. N. Oliveira, ‘Viscoelasticity of blood and viscoelastic blood analogues for use in polydymethylsiloxane in vitro models of the circulatory system’, *Biomicrofluidics*, vol. 7, no. 3, May 2013, doi: 10.1063/1.4804649.
[64] K. W. Q. Low, R. van Loon, S. Rolland, and J. Sienz, ‘Formulation of Generalized Mass Transfer Correlations for Blood Oxygenator Design’, *J. Biomech. Eng.*, vol. 139, pp. 1–16, Mar. 2017, doi: 10.1115/1.4035535.
[65] L. Novakova, ‘Deformation correction algorithm for PIV data’, presented at the THE MEETING OF DEPARTMENTS OF FLUID MECHANICS AND THERMOMECHANICS (35MDFMT): Proceedings of the 35th Meeting of Departments of Fluid Mechanics and Thermomechanics, Šamorín – Čilistov, Slovak Republic, 2016, p. 020008, doi: 10.1063/1.4963030.